Some Insights into the Characteristics and Dynamics of the Chilean Low-Level Coastal Jet

QINGFANG JIANG

University Corporation for Atmospheric Research, Monterey, California

SHOUPING WANG AND LARRY O'NEILL

Naval Research Laboratory, Monterey, California

ABSTRACT

The characteristics and dynamics of the Chilean low-level coastal jet (CLLCJ) are examined here through diagnosing real-time mesoscale model forecasts in support of the Variability of the American Monsoon System (VAMOS) Ocean–Cloud–Atmosphere Land Study (VOCALS) and additional sensitivity simulations. The forecasted surface winds over the southeast Pacific compare favorably with available observations. According to the forecasts and sensitivity simulations, the Southeast Pacific high pressure system (SEPH) plays a primary role in driving the CLLCJ. The Andes significantly intensify the CLLCJ mainly through interacting with the SEPH and anchoring a baroclinic zone along the Chilean coast. The land–sea differential heating also enhances the CLLCJ by strengthening the coastal baroclinic zone. Based on the location of the SEPH center, the CLLCJ can be separated into two types: a strong-forcing jet, with the SEPH close to the central Chilean coastline; and a weak-forcing jet, with the SEPH centered far away from the coastline. The former is much more intense and associated with stronger interaction between the SEPH and the Andes.

The CLLCJ is slightly supergeostrophic within the marine boundary layer top inversion, where weak easterlies develop, and subgeostrophic in the turbulent boundary layer below, where westerlies are present. The inversion easterlies induce strong subsidence along the coast, which contributes to the formation of the coastal low and the coastal baroclinic zone.

1. Introduction

Satellite observations and numerical modeling studies have shown that a low-level equatorward jet frequently occurs offshore of the central Chilean coast [i.e., the Chilean low-level coastal jet (CLLCJ)] under the influence of the semipermanent Southeast Pacific high pressure (SEPH) system (Fig. 1). The definitions, characteristics, and formation mechanisms of a variety of low-level jets have been reviewed by Stensrud (1996). In this study, we define a coastal low-level jet as a low-level wind maxima oriented nearly parallel to the coastline with appreciable vertical and horizontal wind shears. The Humboldt Current system along the west coast of South America is one of the most productive marine ecosystems on the earth, largely due to the intense coastal upwelling driven by the CLLCJ, which brings up cool and nutrient-rich waters to the surface (Bakun and Nelson 1991). The cold sea surface temperature (SST) anomaly associated with the upwelling is believed to play a key role in generating the persistent stratocumulus deck over the southeast Pacific (SEP). The CLLCJ is typically located between 25° and 35°S, with a surface wind speed maximum extending a few hundred kilometers offshore (Josey et al. 2002). Some climatological aspects of the CLLCJ have been examined by Garreaud and Muñoz (2005) using 4-yr Quick Scatterometer (QuikSCAT) surface winds, complemented with mesoscale model simulations. They found that, while the CLLCJ occurs in all seasons, it takes place more often in the austral spring and summer, more than 60% of the time. The jet axis is located approximately 150 km from the coastline and the wind speed maximum exceeds 8 m s^{-1} in winter, spring, and summer seasonal means. In a companion paper, Muñoz and Garreaud (2005) diagnosed the momentum budget in

Corresponding author address: Qingfang Jiang, University Co-operation for Atmospheric Research, 7 Grace Hopper Ave., Monterey, CA 93940-5502.
E-mail: jiang@nrlmry.navy.mil

		Form Approved OMB No. 0704-0188

Report Documentation Page

1. REPORT DATE **MAR 2010**	2. REPORT TYPE	3. DATES COVERED **00-00-2010 to 00-00-2010**
4. TITLE AND SUBTITLE **Some Insights into the Characteristics and Dynamics of the Chilean Low-Level Coastal Jet**		5a. CONTRACT NUMBER
		5b. GRANT NUMBER
		5c. PROGRAM ELEMENT NUMBER
6. AUTHOR(S)		5d. PROJECT NUMBER
		5e. TASK NUMBER
		5f. WORK UNIT NUMBER
7. PERFORMING ORGANIZATION NAME(S) AND ADDRESS(ES) **Naval Research Laboratory,Monterey,CA,93943**		8. PERFORMING ORGANIZATION REPORT NUMBER
9. SPONSORING/MONITORING AGENCY NAME(S) AND ADDRESS(ES)		10. SPONSOR/MONITOR'S ACRONYM(S)
		11. SPONSOR/MONITOR'S REPORT NUMBER(S)

12. DISTRIBUTION/AVAILABILITY STATEMENT
Approved for public release; distribution unlimited

13. SUPPLEMENTARY NOTES

14. ABSTRACT

The characteristics and dynamics of the Chilean low-level coastal jet (CLLCJ) are examined here through diagnosing real-time mesoscale model forecasts in support of the Variability of the American Monsoon System (VAMOS) Ocean?Cloud?Atmosphere Land Study (VOCALS) and additional sensitivity simulations. The forecasted surface winds over the southeast Pacific compare favorably with available observations. According to the forecasts and sensitivity simulations, the Southeast Pacific high pressure system(SEPH) plays a primary role in driving the CLLCJ. The Andes significantly intensify the CLLCJ mainly through interacting with the SEPH and anchoring a baroclinic zone along the Chilean coast. The land?sea differential heating also enhances the CLLCJ by strengthening the coastal baroclinic zone. Based on the location of the SEPH center the CLLCJ can be separated into two types: a strong-forcing jet, with the SEPH close to the central Chilean coastline; and a weak-forcing jet, with the SEPHcentered far away fromthe coastline. The former is muchmore intense and associated with stronger interaction between the SEPH and the Andes. The CLLCJ is slightly supergeostrophic within the marine boundary layer top inversion, where weak easterlies develop, and subgeostrophic in the turbulent boundary layer below, where westerlies are present. The inversion easterlies induce strong subsidence along the coast, which contributes to the formation of the coastal low and the coastal baroclinic zone.

15. SUBJECT TERMS

16. SECURITY CLASSIFICATION OF:			17. LIMITATION OF ABSTRACT	18. NUMBER OF PAGES	19a. NAME OF RESPONSIBLE PERSON
a. REPORT **unclassified**	b. ABSTRACT **unclassified**	c. THIS PAGE **unclassified**	**Same as Report (SAR)**	**22**	

Standard Form 298 (Rev. 8-98)
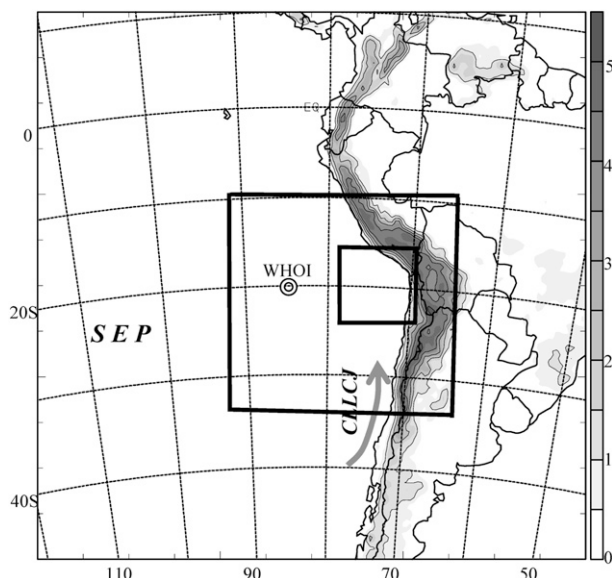Prescribed by ANSI Std Z39-18

FIG. 1. Terrain height in the 45-km grid domain is shown in grayscale (interval = 0.5 km). The bold squares correspond to the 15-km and 5-km grid domains and the gray arrow indicates the location of the CLLCJ. The location of the WHOI buoy is labeled.

the CLLCJ using output from 20-day mesoscale numerical simulations and found that near the marine boundary layer (MBL) top, the flow is approximately in geostrophic balance. They also suggested that the Andes, which extend well above the inversion, could serve as a wall to preclude the development of strong low-level easterly flow. Muñoz (2008) investigated the diurnal variation of the surface winds over the SEP and concluded that the diurnal variation of the surface winds over the SEP maximizes between 20° and 30°S rather than over the CLLCJ itself.

The CLLCJ bears remarkable similarities to its Northern Hemisphere counterpart, the low-level jet offshore of the California coast [i.e., the California coastal jet (CCJ)], which has received much more attention (e.g., Chao 1985; Burk and Thompson 1996; Cui et al. 1998; Pomeroy and Parish 2001). For example, both jets are equatorward and oriented nearly parallel to the coastlines under the influence of subtropical Pacific high pressure systems. The jet cores are located within the MBL top inversion, associated with a downward sloping of the inversion toward the coast. A few dynamical mechanisms regarding the formation of the California coastal jet have been proposed. Using an analytical shallow-water model, Chao (1985) has demonstrated that the inhibition of a geostrophically balanced westerly flow by the Andes near 40°S could create an equatorward coastal jet somewhat resembling the observed California coastal jet. In a numerical study of a summertime California coastal jet

event, Burk and Thompson (1996) attributed the formation of the CCJ to the subtropical Pacific high pressure and the coastal baroclinicity associated with land–sea differential heating. Bakun (1990) hypothesized that in general land–sea differential heating (LSDH) increases the low-level alongshore flow. Pomeroy and Parish (2001) analyzed aircraft in situ measurements of a CCJ event and speculated that the CCJ and the attendant sloping MBL top inversion are induced by a geostrophic adjustment process associated with the horizontal temperature contrast between the cool ocean and warm continent. Muñoz and Garreaud (2005) noted that their results suggest the controlling physical processes for the CLLCJ are similar to those proposed by Chao (1985). These studies suggested three key players in the formation of these subtropical coastal jets: the subtropical high pressure system, coastal topography, and LSDH, the effects of which will be evaluated in this study. It is also noteworthy that hydraulic theory has been used extensively to interpret the MBL flow response to the California coastal terrain (e.g., Rogerson 1999; Haack and Burk 2001).

This study is motivated by a recently completed field campaign, the Variability of the American Monsoon System (VAMOS) Ocean–Cloud–Atmosphere Land Study (VOCALS). One of the primary VOCALS objectives is to understand the SEP regional climate associated with the coupling between the upper ocean, the land, and the atmosphere (Woods et al. 2007). VOCALS comprises two components: the modeling component (VOCALS-Mod), and the regional experiment component (VOCALS-Rex), which took place in October and November of 2008. In addition to land-based, buoy, and satellite observations, in situ and remote sensing measurements were conducted by six instrumented research aircraft and two research ships during the two-month observational period. Although most observations were obtained within the VOCALS target area (approximately the area of the 5-km grid domain in Fig. 1), which is located to the north of the CLLCJ, these observations provide valuable data for model validation over this relatively data-sparse region. During the field observation period, the atmospheric component of the Coupled Ocean–Atmosphere Mesoscale Prediction System (COAMPS;[1] Hodur 1997) and a number of other mesoscale and global models had been applied over South America and the SEP to provide real-time forecast support for the VOCALS-Rex operation planning. In this study, the 3-hourly output from COAMPS twice-daily 48-h forecasts during the VOCALS-Rex period will be examined, complemented with additional sensitivity

---

[1] COAMPS is a registered trademark of the Naval Research Laboratory.

simulations to deepen our understanding of the characteristics and dynamics of the CLLCJ.

The remainder of this paper is organized as follows. In section 2, the COAMPS model and the model configuration for the real-time forecast are described. The simulated surface winds and temperature are compared with satellite and buoy observations. The characteristics of the CLLCJ are illustrated in section 3 using the 3-hourly output from the COAMPS forecasts. In section 4, two selected CLLCJ events are further examined through trajectory analysis and diagnosis of sensitivity simulations with varying terrain heights and sensible surface heat fluxes. Section 5 contains discussions of relevant dynamics and conclusions.

2. COAMPS real-time forecast

a. Numerical aspects

COAMPS is a fully compressible, nonhydrostatic terrain-following mesoscale model. The boundary layer and free-atmospheric turbulent mixing are represented using a prognostic equation for the turbulence kinetic energy (TKE) (Mellor and Yamada 1974):

$$\frac{De}{Dt} = \frac{\partial}{\partial z}\left(Se\frac{\partial e}{\partial z}\right) - \overline{u'w'}\frac{\partial \mathbf{U}}{\partial z} - \overline{v'w'}\frac{\partial \mathbf{V}}{\partial z} + g\beta\overline{w'\theta'}$$
$$- \frac{\Gamma}{l_m}e^{3/2} + D_e,$$

where $e = (\overline{u'^2} + \overline{v'^2} + \overline{w'^2})/2$ is the turbulence kinetic energy; $(\mathbf{U}, \mathbf{V})$ and (u', v', w') denote grid-scale horizontal wind vectors and turbulent fluctuations, respectively; β is thermal expansion coefficient; S and Γ are constants; l_m is the mixing length formulated based on Mellor and Yamada (1974) and Thompson and Burk (1991); and D_e represents the subgrid-scale TKE mixing. The overbars represent ensemble average. The subgrid-scale mixing of momentum and heat fluxes is parameterized as $(\overline{u'w'}, \overline{v'w'}) = -K_M(\partial \mathbf{U}/\partial z, \partial \mathbf{V}/\partial z)$ and $\overline{w'\theta'} = -K_H\partial\theta/\partial z$, where K_M and K_H are eddy mixing coefficients of momentum and heat fluxes given by $K_{M,H} = S_{M,H}l_m(2e)^{1/2}$ and $S_{M,H}$ are constants. The surface heat and momentum fluxes are computed following the Wang et al. (2002) formulation, which is a modified version of Fairall et al. (1996). The grid-scale evolution of the moist processes is explicitly predicted from budget equations for cloud water, cloud ice, rainwater, snowflakes, and water vapor (Rutledge and Hobbs 1983) and the subgrid-scale moist convective processes are parameterized using an approach following Kain and Fritsch (1993). Fu–Liou's δ-four-stream approximation is used for the short- and longwave radiation processes (Fu et al. 1997; Liu et al. 2009).

The initial model fields are created from multivariate optimum interpolation analysis of upper-air sounding, surface, commercial aircraft, and satellite data that are quality controlled and blended with the 12-h COAMPS forecast fields. Lateral boundary conditions for the outermost grid mesh are derived from Navy Operational Global Analysis and Prediction System (NOGAPS) forecast fields. The computational domain contains three horizontally nested grid meshes of 151 × 151, 199 × 181, and 181 × 181 grid points with horizontal grid spacings of 45, 15, and 5 km, respectively. The innermost domain is coincident with the VOCALS intensive observation area, which is located to the north of the CLLCJ (Fig. 1). The 15-km grid captures only the northern portion of the CLLCJ. Therefore, the 45-km grid data is used for characterizing the CLLCJ in this study. There are 45 levels in the vertical on a nonuniform sigma grid with 26 levels in the lowest 2.6 km. The model top is located approximately at 30 km ASL and a sponge upper boundary condition is applied to the upper one-third of the domain to reduce the reflection of gravity waves. The terrain data is based on the Global Land One-km Base Elevation (GLOBE) dataset and the terrain in the 45-km mesh is shown in Fig. 1. The model was initialized at 0000 and 1200 UTC, respectively, and the twice-daily 48-h forecasts were provided from 20 October to 30 November 2008. Only the output from the 6–18-h period of each forecast is used for this study.

b. Model validation

To evaluate the model performance, the 40-day COAMPS real-time forecasts have been compared extensively with a variety of observations obtained from the VOCALS-REX. In general, the agreement between the COAMPS forecasts and the available observations is encouraging (Wang et al. 2010, manuscript submitted to *Atmos. Chem. Phys.*). As an example, the 40-day-average 10-m winds from the COAMPS 45-km grid and the QuikSCAT 10-m winds averaged over the same period are shown in Fig. 2. SeaWinds on QuikSCAT measures radar backscatter from the ocean surface, which is used to derive vector wind stress. The 10-m winds (referred to as surface winds hereafter) are estimated using a geophysical model function that relates the backscatter to 10-m equivalent neutral wind, the wind that would exist in a neutrally stable near-surface atmosphere over a motionless surface (Liu and Tang 1996). The difference between the equivalent neutral and actual 10-m wind speeds is generally less than 0.2 m s^{-1} (Mears et al. 2001; Ebuchi et al. 2002; Portabella and Stoffelen 2009) and will thus be neglected here in comparing the QuikSCAT winds with the COAMPS winds. The QuikSCAT observations show that, during the
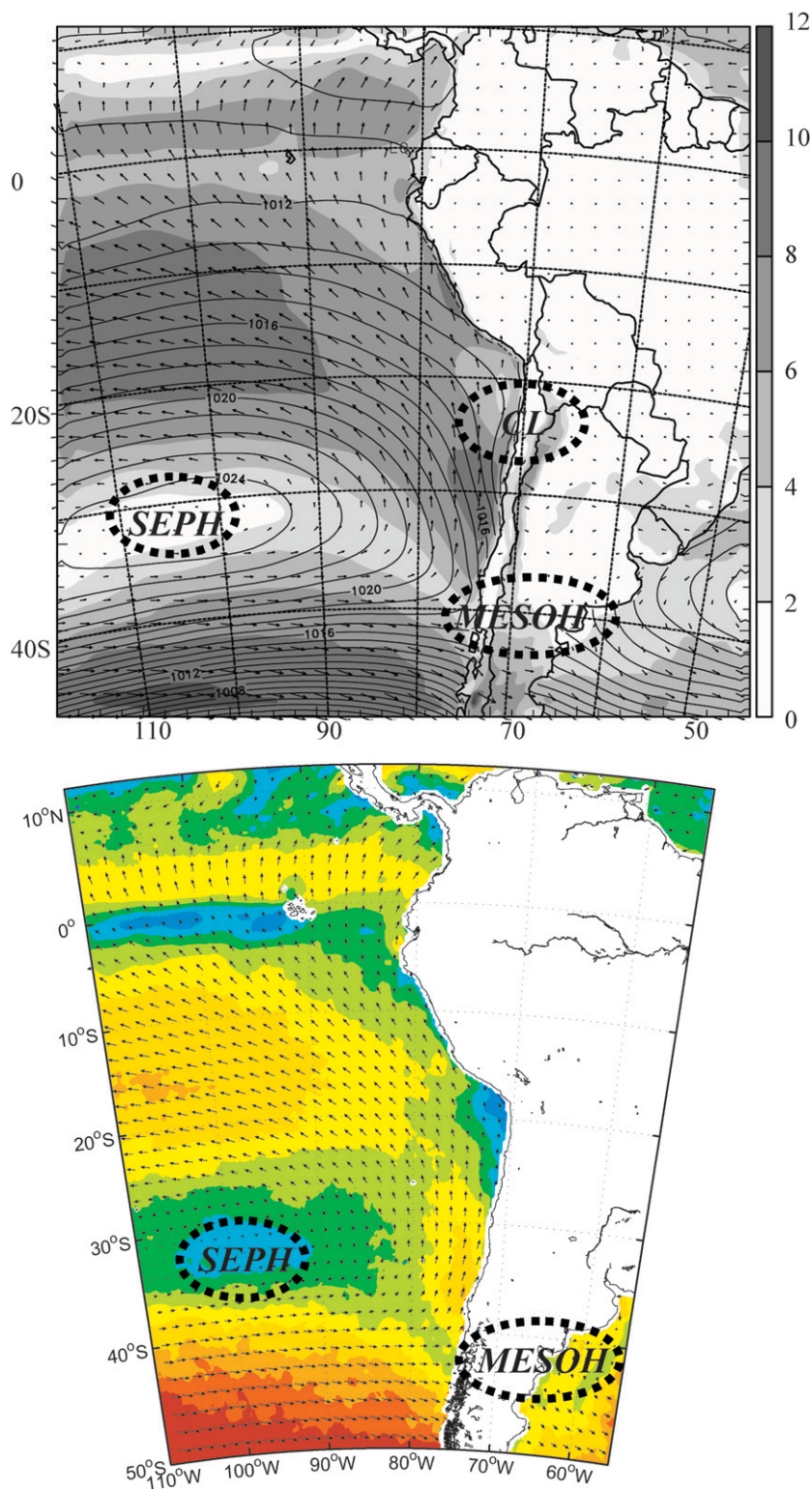
FIG. 2. The 40-day average 10-m wind speed (grayscale, increment = 2 m s^{-1}), wind vectors, and surface pressure (contours, increment = 1 hPa) from (top) the COAMPS real-time forecasts and (bottom) the corresponding average wind speed and wind vectors derived from the QuikSCAT data. The locations of the SEPH, MESOH, and CL are highlighted.

VOCALS field observational period, the mean low-level winds over the SEP are characterized by an anticyclonic circulation around a weak wind zone centered approximately at 32°S, 105°W, coincided with the center of the SEPH as evident in the COAMPS 40-day-average pressure field (Fig. 2a). Within the model domain, the QuikSCAT winds indicate the presence of three branches of the anticyclonic circulation: the midlatitude westerlies, the coastal southerlies between 40° and 25°S (i.e., CLLCJ), and the widespread southeasterlies to the north of 25°S. COAMPS reproduces well these three branches and the simulated wind direction and wind speed show reasonable qualitative agreement with the QuikSCAT winds. Along the Chilean and Peruvian coast, the surface winds are characterized by a weak wind zone near 40°S, which separates the midlatitude westerlies to the south and the southerly coastal jet to the north, and a nearly calm zone located to the north of the CLLCJ near the Peru and Chile border, where the main Andes ridge exhibits a concave shape. The COAMPS forecasts reproduce the two weak flow zones. According to COAMPS, the southern weak wind zone near 40°S is associated with a mesoscale high pressure corresponding to the intersection of the SEPH ridge axis with the Chilean coastline [referred to as the mesoscale high pressure (MESOH)], likely due to the blocking of the westerlies by the Andes. It is interesting that while the major axis of the SEPH is oriented slightly southwest–northeast, the pressure ridge tilts northwest–southeast toward the coastline, suggesting strong interaction between the SEPH and the Andes near 40°S. To the northwest of the surface the CLLCJ maximum, a coastal low pressure zone (referred to as CL) is evident, the characteristics of which have been illustrated by Garreaud et al. (2002) and Garreaud and Rutllant (2003).

The COAMPS-simulated winds and temperature have also been compared with the available Woods Hole Oceanographic Institution (WHOI) buoy measurements during the same time period (Fig. 3). The WHOI buoy, located at 20°S, 85°W (Fig. 1), documented the surface winds and temperature for 37 days of the 40-day COAMPS real-time forecast period. The prevailing surface winds are southeasterly at the WHOI buoy location (i.e., in the southeasterly flow branch of the circulation, Fig. 2). The observed winds exhibit both synoptic-scale (i.e., from a few days up to about a week) and diurnal variations, which are well captured by COAMPS. The temperature shows a slow warming trend with time and weak diurnal variation. Noticeably, there is a cold bias around mid-November, which is consistent with the southeasterly bias in the wind fields during the same period. The biases and RMS error for the zonal and meridional wind components are 0.67/1.4 and $-1.2/1.7$ m s^{-1}, respectively. The COAMPS forecasted air temperature is
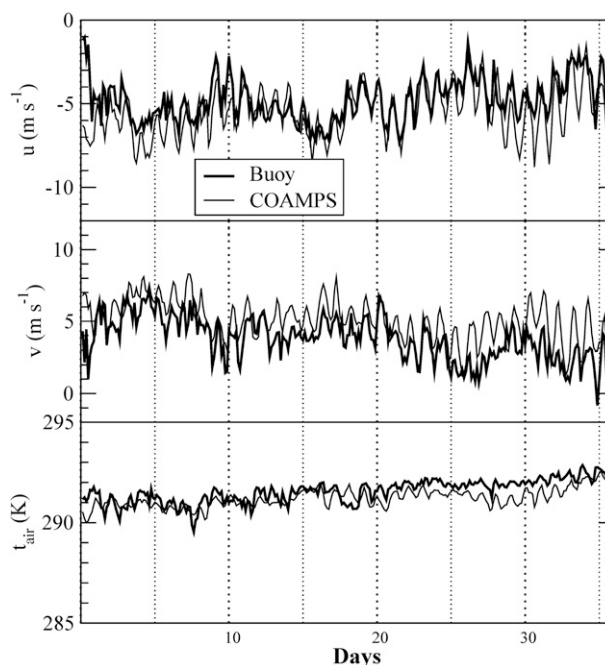

FIG. 3. Time series of u and v wind components and surface temperature derived form the WHOI buoy measurement for 37 days in October and November 2008. The corresponding COAMPS simulated fields are included for comparison.

also in good agreement with the buoy observations with a bias and RMS error of 0.34/0.54 K, respectively.

In summary, we find that the COAMPS real-time forecasted surface winds and temperature compare favorably with those observed by QuikSCAT and the WHOI buoy. The COAMPS-forecasted winds, temperature, moisture, clouds, and boundary layer height have also been compared with other available observations such as research aircraft in situ measurements, radiosonde data, and research ship measurements in Wang et al. (2010, manuscript submitted to *Atmos. Chem. Phys.*). They found that the overall performance of COAMPS was satisfactory. Especially, the simulated low-level winds and temperature agree with the available observations particularly well. However, they also noticed that the simulated boundary layer in general was shallower than observations near the coast.

3. Classification and characteristics of CLLCJ

The encouraging agreement between the COAMPS real-time forecasts and available observations allows us to further examine the characteristics of the low-level jet and the associated dynamics using the COAMPS real-time forecast output. Particularly, we are interested in the temporal evolution of the CLLCJ, the mean low-level jet
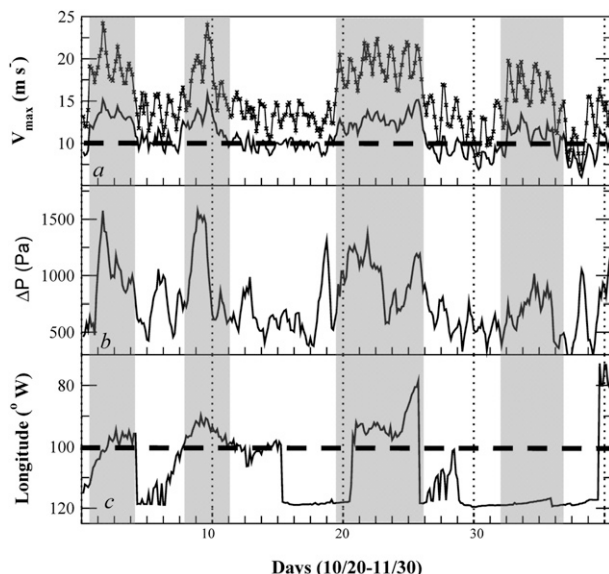
FIG. 4. Time series of (a) the meridional wind component maximum at the surface (bold) and in the lowest 2 km (thin curve with crosses) in the CLLCJ (Fig. 1), (b) the surface pressure difference between MESOH and along the Chilean coast between 20° and 40°S, and (c) the longitude of the SEPH center derived from COAMPS real-time forecasts. The four CLLCJ events are shaded with light gray. The bold, dashed lines in (a) and (c) correspond to 10 m s^{-1} and 100°W, respectively.

structure, and the connection between the SEPH and the CLLCJ.

The evolution of the CLLCJ maxima at the surface and within the lowest 2 km, offshore of the central Chilean coast (i.e., between 20° and 40°S) is shown in Fig. 4a. The surface southerly winds are around or above 10 m s^{-1} for most days, and exhibit strong diurnal and synoptic-scale variations. The diurnal variation of the CLLCJ or CCJ has been examined by several groups (e.g., Burk and Thompson 1996; Muñoz 2008) and is beyond the scope of this study. Four strong CLLCJ periods (hereafter referred to as CLLCJ events) are evident with surface southerlies persistently greater than 10 m s^{-1}, each lasting from 3 days to 1 week, as highlighted by the gray shading in Fig. 4. Aloft, the southerly wind maximum (i.e., the jet core), located in the MBL inversion, is approximately 1.5–2 times of the corresponding maximum at the surface during the 4 events.

Also shown in Fig. 4b is the maximum surface pressure difference along the coastline between the MESOH near 40°S and the coastal low (CL) to the north of the jet, an index for the meridional pressure gradient. In addition to the diurnal variation, this south–north pressure difference clearly shows four maxima, approximately corresponding to the four CLLCJ events. Further inspection reveals that the maximum surface wind speed

in the CLLCJ is positively correlated with the south–north surface pressure difference between the mesoscale high and the coastal low along the central Chilean coastline, implying the crucial role that the meridional pressure gradient plays in enhancing the CLLCJ.

It is evident that the longitudinal locations of the SEPH center are characterized by a bimodal distribution during the 40-day period (Fig. 4c), namely nearshore locations (i.e., to the east of 100°W or within 2500 km from the coast) and far offshore locations (i.e., near 120°W, where the western model boundary of is located). During the first three low-level jet events, the south–north pressure difference reaches a maximum and the SEPH is centered closer the coastline, implying connections between the SEPH center location, the south–north pressure gradient, and the CLLCJ intensity. These connections also suggest that the longitudinal location of the SEPH center may be a useful index for the synoptic-scale forcing. We further hypothesize that the closer the SEPH is to the coastline, the stronger the synoptic forcing on the CLLCJ. To test the hypothesis, we separate the 40-day period into two periods: the ''strong forcing'' period with the SEPH centered to the east of 100°W, and the ''weak forcing'' period with the SEPH centered to the west of 100°W. The strong-forcing and weak-forcing periods account for 36% and 64% of the time, respectively. Note that these percentages are relatively insensitive to the choice of the threshold longitude. The surface jet and synoptic-scale patterns are strikingly different for these two periods (Fig. 5), consistent with our hypothesis that the location of the SEP predominantly controls the strength of the CLLCJ. For the strong-forcing period, the mean SEPH is centered near 95°W, ~2000 km offshore. The CLLCJ is approximately 1500 km in length, located between 25° and 40°S with a surface maximum near 36°S. For the weak-forcing period, the mean center of the SEPH is located to the west of the model domain and the surface pressure gradient offshore of central Chile is noticeably weaker than the strong-forcing period. The surface CLLCJ is substantially shorter, weaker, and centered farther north compared to the strong-forcing period. At the 5-km level, the strong-forcing period is characterized by a shortwave pressure ridge located right over the surface SEPH center and a pressure trough extends over the CLLCJ. For the weak-forcing period, the pressure field is more uniform in the zonal direction.

The surface winds derived from QuikSCAT are also averaged over the strong-forcing and weak-forcing periods separately (Figs. 5c,d). For the strong-forcing period, the surface winds are characterized by a weak wind zone centered approximately at 33°S, 95°W, in agreement with the location of the SEPH center deduced from COAMPS forecasts averaged over the same period
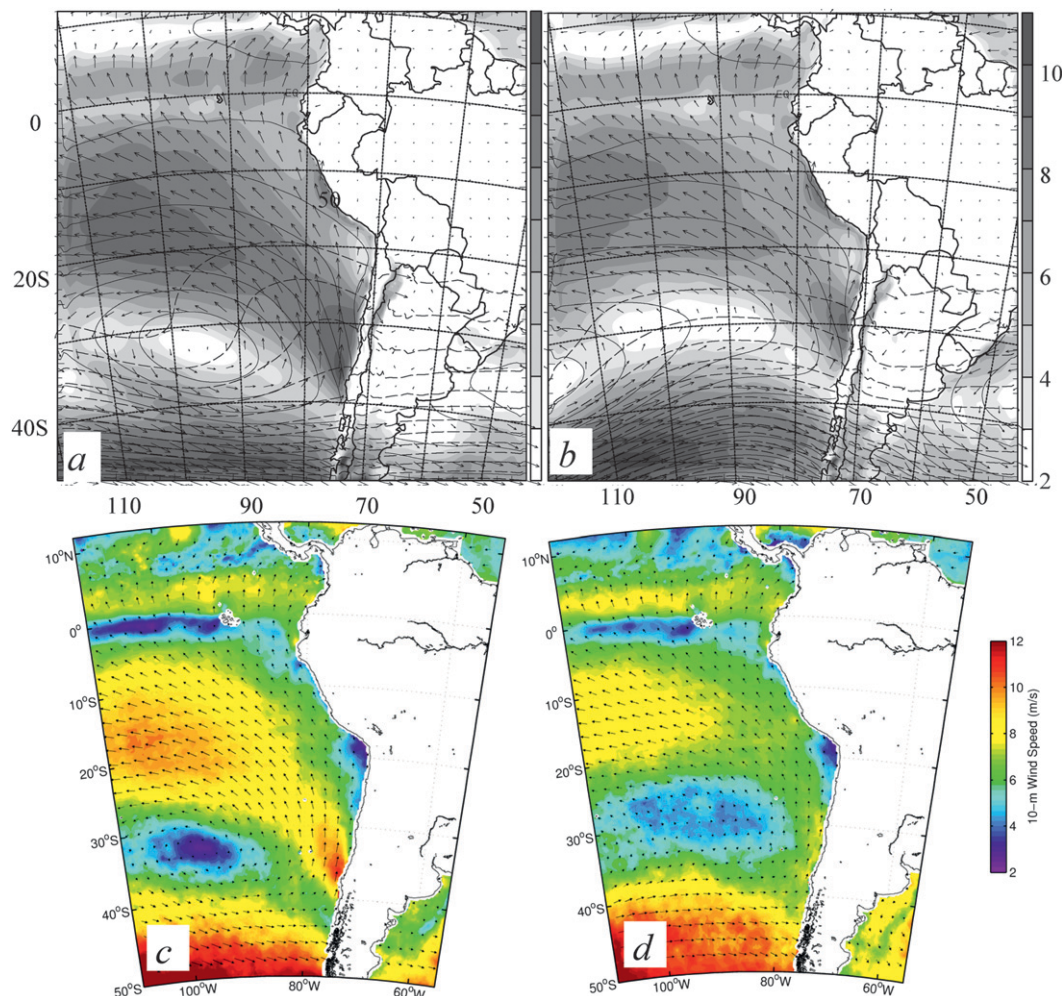
FIG. 5. The 10-m wind speed (grayscale, increment $= 1$ m s^{-1}) and wind vectors, surface pressure (contours, increment $= 2$ hPa), and 5 km MSL pressure (dashed contours, increment $= 2$ hPa) averaged over (a) strong-forcing period and (b) weak-forcing period. (c),(d) The QuikSCAT wind speed (color shading, increment $= 2$ m s^{-1}) averaged over the corresponding periods.

(Fig. 5a). The location, meridional extent, and general structure of the surface CLLCJ simulated by COAMPS agree well with the QuikSCAT surface wind observations for both the weak- and strong-forcing cases, as seen by comparing Figs. 5a,b with 5c,d. The good agreement between the COAMPS surface winds and the QuikSCAT winds averaged over the corresponding periods reinforces our confidence in the COAMPS forecasts.

The differences between the CLLCJ under the two different large-scale forcing patterns are also evident in the vertical cross sections of the alongshore wind component and potential temperature, oriented approximately across the CLLCJ and through the surface wind speed maximum (Fig. 6). The jet core resides at the bottom of the MBL inversion associated with a coastal baroclinic zone, which is evident by the downward

sloping of the inversion toward the coastline. Note that, in this study, we loosely use the term inversion to refer to the relatively thick stable layer above the turbulent BL. The observed instantaneous MBL top inversion can be very thin, especially in the presence of clouds (Wang et al. 2010, manuscript submitted to *Atmos. Chem. Phys.*). The jet extends approximately 1000 km offshore over the ocean, and is significantly stronger during the strong-forcing period than the weak-forcing period (Figs. 6a,b). Over the coastal area, the alongshore wind component is northerly above the inversion, associated with the reversal of the zonal potential temperature gradient. This relatively narrow elevated northerly jet can be traced back to the tropical easterlies, which are deflected southward by the Ecuador and northern Peruvian coastal topography. This elevated jet is almost parallel to the coastline and
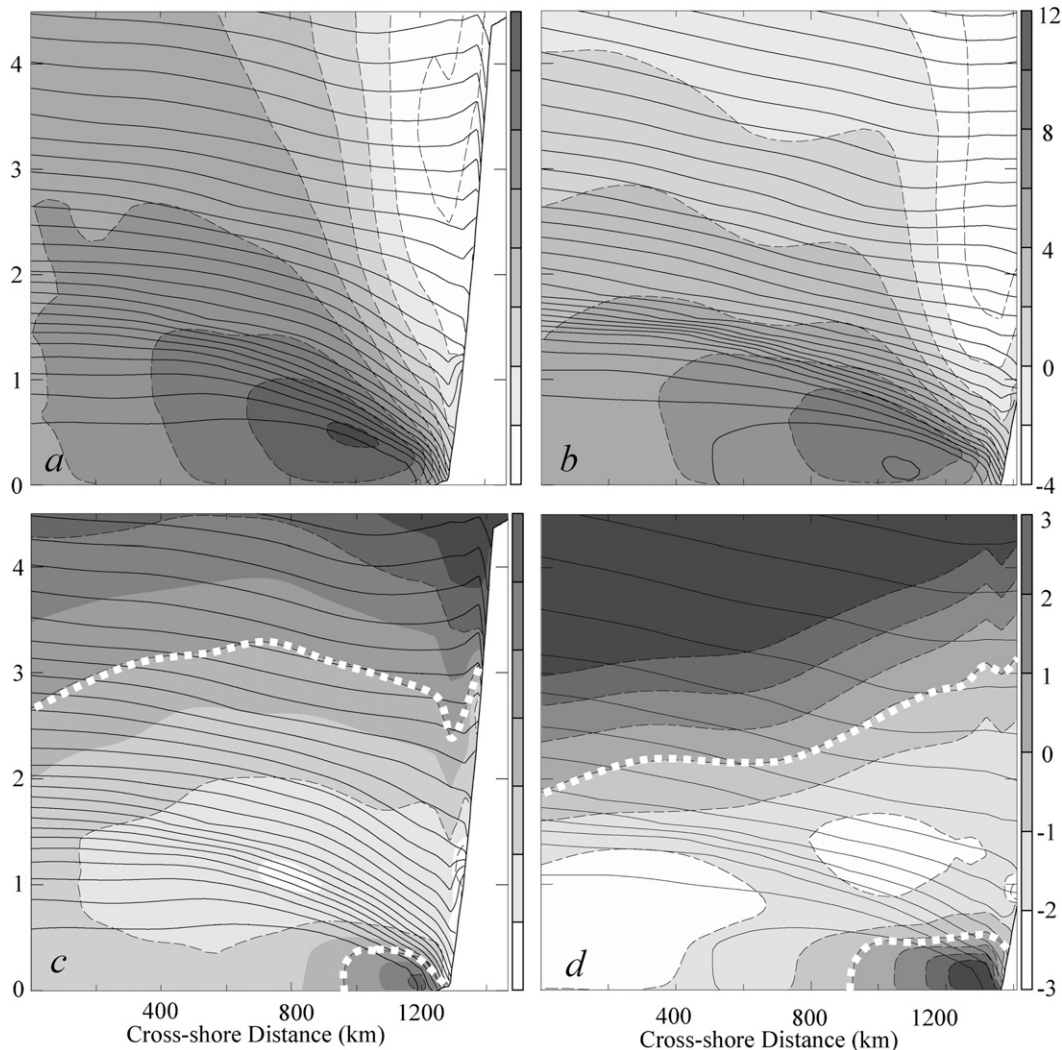
FIG. 6. The alongshore wind component (grayscale and dashed contours, increment $= 2$ m s^{-1}) and potential temperature (solid contours, increment $= 1$ K) in a cross-shore vertical section through the surface wind maximum of the CLLCJ for (a) strong-forcing average and (b) weak-forcing average. (c),(d) The zonal wind component (increment $= 1$ m s^{-1}) and potential temperature. The white dashed contours in (c) and (d) correspond to $u = 0$.

often reaches the maximum near 20°S, the dynamics of which will be further examined in a separate paper. As shown in Figs. 6c,d, the cross-shore wind component is characterized by a nearshore westerly flow in the viscous boundary layer and an easterly flow within the MBL top inversion (~0.5–1.5 km). With the steep Andes to the east serving as a nearly vertical wall, the boundary layer top easterlies create a divergence zone, as required by the law of conservation of mass, and therefore, enhance the subsidence along the coast.

Shown in Fig. 7 are the mean profiles of the two horizontal wind components (u, v), and the corresponding meridional geostrophic wind components v_g derived from the pressure field in the lowest 4 km for the weak and strong-forcing periods, respectively. The profiles are

derived by averaging over a 6×6 grid box centered over the mean jet maximum for each period. The boundary layer westerlies and the elevated easterlies in the MBL top inversion between approximately 0.3 and 2 km are evident (Fig. 7c). The meridional wind component is approximately in geostrophic balance above the turbulent boundary layer as found by previous studies of the CLLCJ and its Northern Hemisphere counterpart, the California coastal jet (e.g., Bielli et al. 2002; Muñoz and Garreaud 2005). However, a careful inspection shows that, within the boundary layer top inversion, the meridional wind is slightly supergeostrophic. The CLLCJ is nearly straight and the centrifugal force is thus negligible, and the resultant east-pointing force likely contributes to the formation of the weak easterlies in the
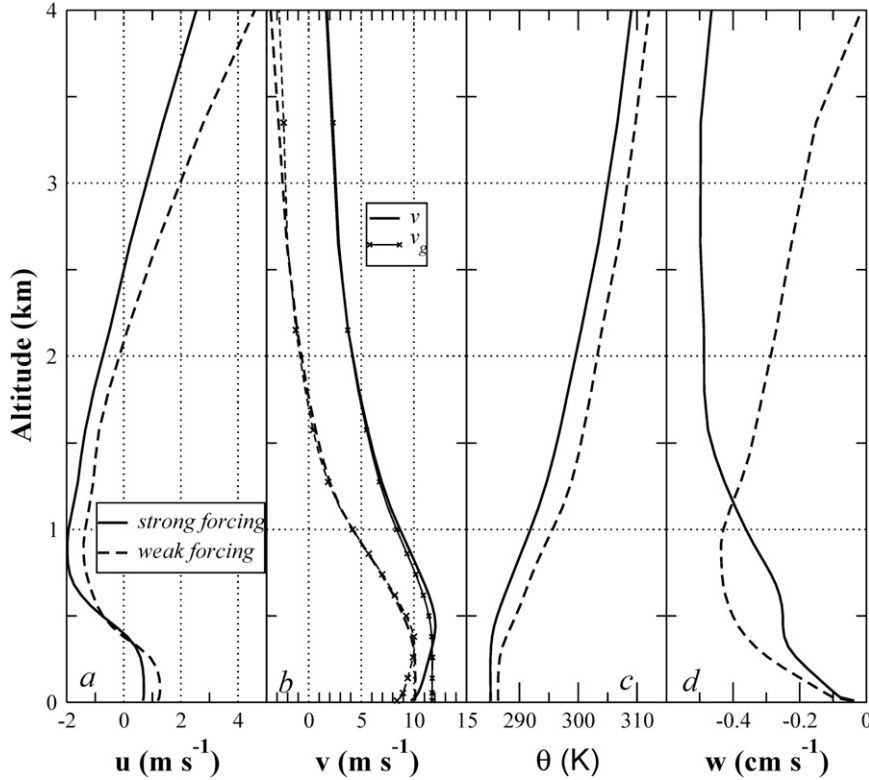
FIG. 7. Profiles of (a) zonal wind component u, (b) meridional wind component v, (c) potential temperature θ, and (d) vertical velocity w averaged over a 6×6 grid square located in the surface wind maxima for the strong-forcing (solid) and weak-forcing (dashed) periods, respectively. The meridional components of the geostrophic winds derived from the pressure are also included in (b) for comparison.

MBL top inversion. Beneath the inversion, the southerly jet is subgeostrophic because of boundary layer friction, and the resultant west-pointing force is consistent with the presence of the westerly flow in the boundary layer.

Following Burk and Thompson (1996), the thermal wind between two reference levels can be estimated using

$$v_t(z) = v(z_{\text{ref}}) - \frac{g}{f\langle T\rangle}\frac{\partial\langle T\rangle}{\partial x}\Delta z \quad \text{and} \quad (1)$$

$$u_t(z) = u(z_{\text{ref}}) + \frac{g}{f\langle T\rangle}\frac{\partial\langle T\rangle}{\partial y}\Delta z, \quad (2)$$

where $\langle T\rangle = \int_z^{z_{\text{ref}}} T\,dz/\Delta z$ is the temperature averaged over the air column between levels z and z_{ref}, $\Delta z = z_{\text{ref}} - z$, f is the Coriolis parameter, and g is the gravitational acceleration. The thermal wind, v_t, computed using (1) with $z_{\text{ref}} = 4$ km, is approximately equal to the geostrophic wind v_g in the lowest 4 km, implying that the CLLCJ is largely in thermal wind balance and owes its existence to the coastal baroclinicity. Figure 7d indicates

pronounced subsidence over the jet. For the strong-forcing period, a much deeper subsidence layer is present compared to the weak-forcing period.

Thermal wind vectors estimated using (1)–(2) with $z = 0$, $z_{\text{ref}} = 2$ km, and $v_t(z_{\text{ref}}) = 0$ (Fig. 8) serve as a measure of the flow baroclinicity in the lowest 2 km; a larger meridional (zonal) thermal wind component corresponds to a stronger zonal (meridional) temperature gradient. For both the weak-forcing and strong-forcing periods, a pronounced cross-shore baroclinic zone is evident, oriented along the Chilean coastline with a characteristic width of 500 km. Thermal winds along the Chilean coast qualitatively resemble the CLLCJ, implying that the CLLCJ is largely a low-level baroclinic jet. The large easterly thermal wind component in the vicinity of the MESOH (Figs. 8a,b) is absent in the 500-m level winds (Figs. 8c,d), suggesting that the winds are strongly ageostrophic near the MESOH. Over the CLLCJ, a narrow (~100 km) divergence zone is present following the coastline (Figs. 8a,b), indicative of strong coastal subsidence, which presumably contributes to the formation of the coastal baroclinic zone. The coastal divergence
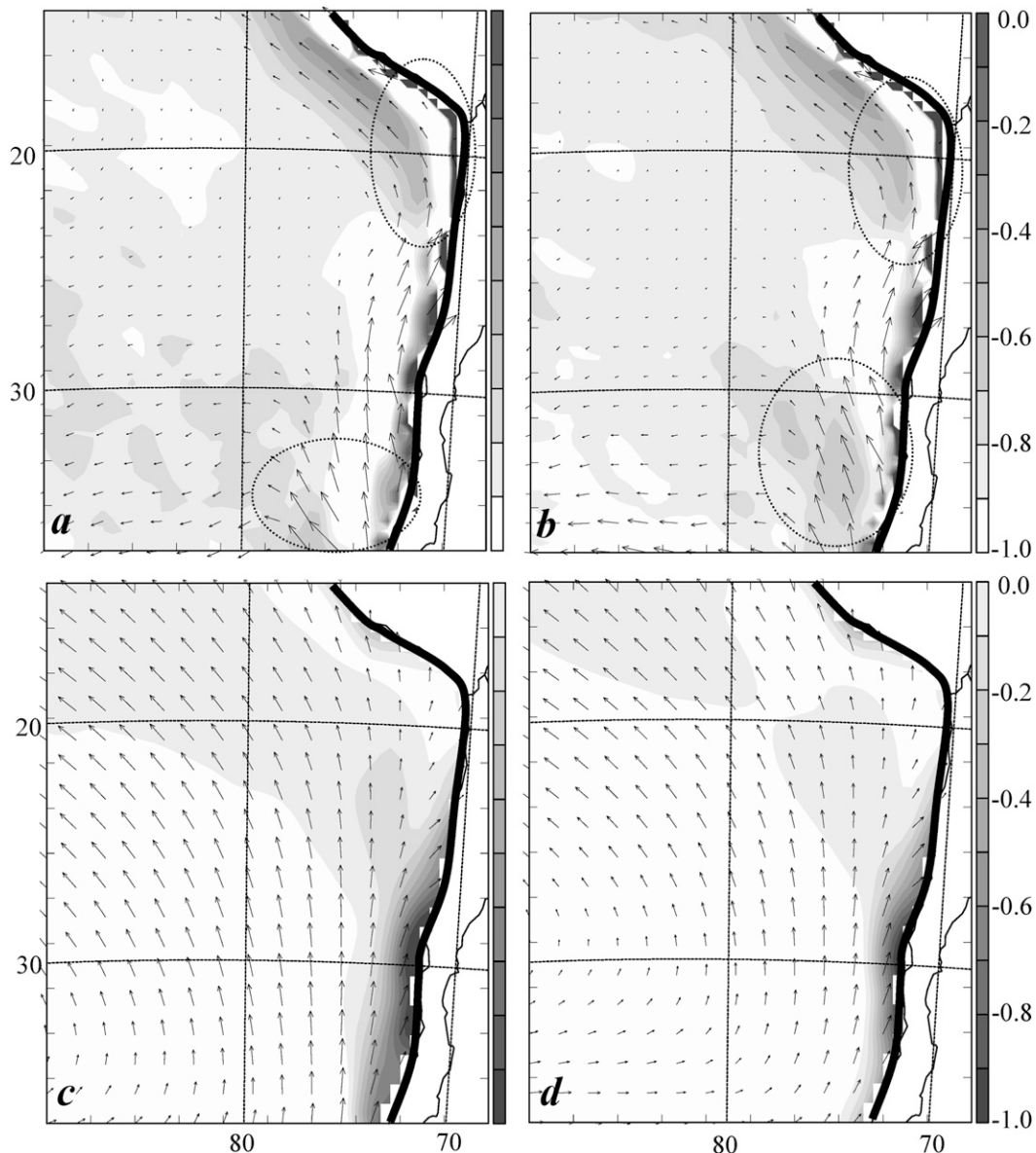
FIG. 8. The divergence (grayscale, increment = 0.1×10^{-5} s^{-1}) at 500 m MSL and thermal winds (vectors, maximum corresponds to 20 m s^{-1}) in the lowest 2 km computed using (1)–(2) for the (a) strong-forcing and (b) weak-forcing means. The wind stress curl (grayscale, interval = 0.1×10^{-6} N m^{-3}) and average wind vectors at 500 m MSL for the (c) strong-forcing and (d) weak-forcing periods. Only the CLLCJ portion of the domain is shown. The MESOH and CL locations are highlighted by dashed ellipses in (a) and (b).

zone changes sign around 23°S, to the north of which, a convergence zone exists along the coastline companied with a widespread divergence zone farther offshore. This alternation of convergence and divergence along the Peru coastline is consistent with satellite observations (not shown).

The wind-driven upwelling rate w in the ocean is proportional to the curl of the surface wind stress τ (i.e., $\rho_w w = -\mathbf{k} \cdot \nabla \times \tau / f$, where ρ_w is the water density).

Shown in Figs. 8c,d is the wind stress curl averaged over the strong- and weak-forcing periods, respectively. It is evident that, during the strong-forcing period, the CLLCJ induces stronger upwelling along the coast and the up-welling zone is substantially larger than the weak-forcing period. The upwelling rate integrated over a swath within 500 km of the coast and between 20° and 40°S for the strong-forcing period is approximately twice as large as that for the weak-forcing period.
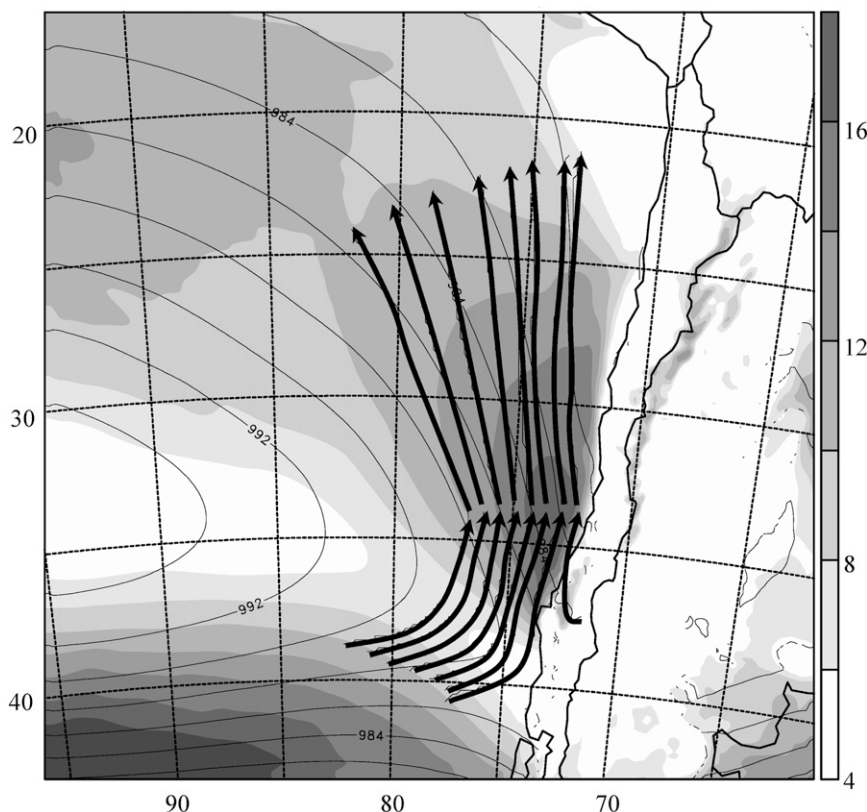
FIG. 9. The 24-h mean wind speed (grayscale, increment = 2 m s^{-1}) and isobars (interval = 2 hPa) at 300 m MSL derived from the 22–23 October simulation. Also included are backward trajectories for air parcels launched from 300 m MSL (i.e., set 1) and forward trajectories for air parcels launched from 600 m MSL (i.e., set 3) near the jet maximum.

In summary, the diagnosis of the real-time COAMPS forecasts reveals some interesting characteristics of the CLLCJ, such as a connection between the SEPH center location and the CLLCJ, a correlation between the south–north pressure gradient and the jet strength, the presence of an elevated northerly jet above the coastal marine boundary layer inversion, and the supergeostrophic flow in the MBL inversion. Specifically, the CLLCJ shows substantial differences in characteristics for the strong- and weak-forcing periods. Some of these issues will be further examined in the following sections.

4. Two case studies of the CLLCJ

To deepen our understanding of the coastal jet formation and adjustment processes, two CLLCJ events corresponding to a strong-forcing period (i.e., 22–23 October) and a weak-forcing period (i.e., 22–23 November), respectively, have been resimulated using a slightly different model configuration. The new model domain is composed of two nested grid mesh of 151 × 151 and 199 × 199 grid points with horizontal spacings of 45 and 15 km,

respectively. The inner domain is centered at (30°S, 85°W), and the new 15-km grid captures the whole CLLCJ. For the 22–23 October (November) event, the model is initialized at 1200 UTC 21 October (21 November), and a 36-h simulation starts at 0000 UTC 22 October (22 November) after a 12-h data assimilation cycle. The first 6 h of each simulation is considered as the model spinup period and the 30-min interval output from the rest 30-h of each simulation is used for the following diagnosis.

According to previous studies, possible controlling factors in the CCJ or CLLCJ formation include synoptic-scale conditions, coastal topography, and LSDH. To evaluate the relative importance of these factors, for each event, in addition to the standard simulation [i.e., the control simulation or (CTRL)], three sensitivity simulations have been performed: the quarter-terrain (QTRN), no-terrain (NTRN), and small sensible heat flux (SSHF) simulations. The terrain height in both the 45- and 15-km meshes is reduced to one-quarter of the true terrain height in the QTRN simulation and set to zero in the NTRN simulation. In the SSHF simulation, the surface sensible heat flux over land is held as constant after

sunrise to minimize the sensible heat flux difference between land and sea (i.e., less than 30 W m^{-2}).

a. Trajectory analysis of the control simulations

To investigate the formation dynamics of the CLLCJ, we perform a trajectory analysis using $\mathbf{x}_{i+1} = \mathbf{x}_i + \mathbf{V}(\mathbf{x}_i)\Delta t$, where $\mathbf{x}_i = (x_i, y_i, z_i)$ and $\mathbf{V}(\mathbf{x}_i) = (u_i, v_i, w_i)$ are the three-dimensional position and velocity vectors at the ith time step, and Δt is the time interval. For this study, $\Delta t = 5$ min or -5 min is used, corresponding to the forward and backward trajectory calculations, respectively. The wind vector $\mathbf{V}(\mathbf{x}_i)$ is obtained from linear interpolation in space and time using the 30-min interval wind output. The air parcel potential temperature, water vapor mixing ratio, and geostrophic winds along each trajectory are also derived in a similar manner. For each simulation, three sets of trajectories are calculated: two sets of backward trajectories with the air parcels launched from a cross section oriented approximately normal to the coastline and through the surface wind maximum and from 300-m (set 1) and 600 m MSL (set 2), respectively, and one set of forward trajectories (set 3) from the same locations as set 2. Each set includes eight trajectories, which are numbered in sequence based on the initial parcel locations from east to west for the convenience of description.

Shown in Fig. 9 are the 300-m 24-h mean wind speed and isobars, superposed with two sets of trajectories calculated using the output from the strong-forcing case (i.e., 22 October). For sets 1 and 2, the air parcels are launched at 2300 UTC 23 October and the backward trajectories are computed over a period of 30 h, or until the trajectory intercepts the underlying topography. The parcels in set 3 are launched at 1800 UTC 22 October and the forward trajectories are calculated for 30-h as well. The coastal MESOH and strong CLLCJ are evident. According to trajectory set 1, the jet air mass comes from two sources. The offshore portion of the CLLCJ originates from the westerlies around 40°S, which turn into southwesterlies near the MESOH. The radii of the trajectory curvature are of the order of 1000 km near MESOH and become significantly larger within the jet (>3000 km). Near the shore, the air mass comes from land. An identical set of air parcels have been launched from 600 m MSL (i.e., set 2), which exhibit similar characteristics except that their trajectories are slightly longer (not shown). Trajectory set 3 indicates that to the north of the jet core the air parcels tend to move away from the coastline and the flow is strongly diffluent. The air parcels at both the 300- and 600-m levels undergo significant descent during their course of acceleration toward the jet maximum (Fig. 10a). This is qualitatively consistent with Garreaud and Rutllant (2003), who found that the CLLCJ "is fed by air parcels
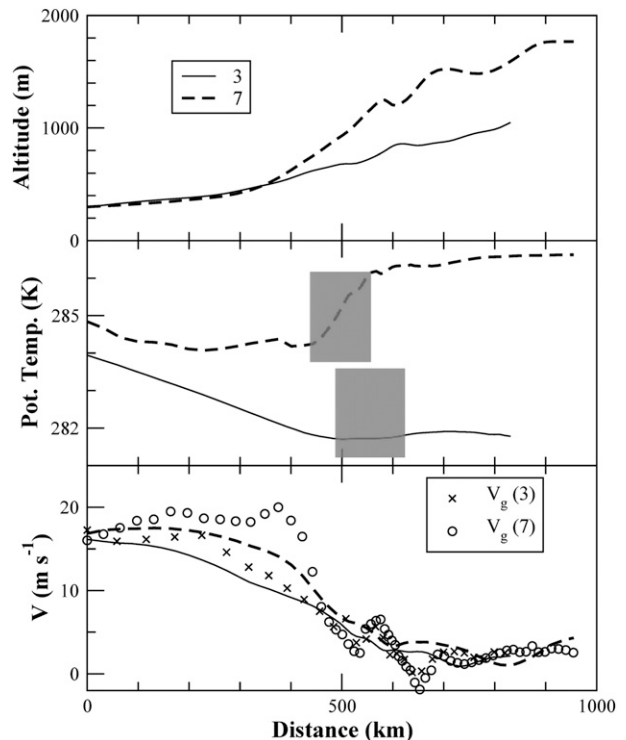

FIG. 10. Plot of altitudes, potential temperatures, and meridional wind components of parcels 3 and 7 from set 1 vs distance for the strong-forcing case. The corresponding meridional geostrophic winds are included as symbols for comparison. The gray boxes indicate the approximate periods that the parcels descend through the MBL inversion.

that 1–2 days before had been located in the middle troposphere over the Pacific Ocean." The variation of the parcel potential temperatures before they are entrained into the MBL is negligible. The potential temperature of parcel 7 drops by 2 K due to cloud evaporation near the BL top. In the MBL, the parcel potential temperatures increase due to vertical mixing and the surface heating as parcels are being advected northward over a progressively warmer sea surface. It is noteworthy that, in general, the closer the parcel is to the coast, the more descent the parcel experiences, and accordingly, the parcel is warmer than parcels at the same level, but farther away from the coast. Parcel 8, which originates over land, experiences the largest descent (~2.5 km) and is the warmest among the eight parcels in set 1 (not shown).

The advection speeds of the parcels are fairly small before they descend into the MBL top inversion. While crossing the inversion, parcels experience a relatively rapid acceleration and the zonal pressure gradient, as measured by v_g, increases simultaneously. Parcel 3 is approximately in geostrophic balance in the BL, and the other two parcels closer to the coast (i.e., 5 and 7) become slightly subgeostrophic after the parcels enter the BL.
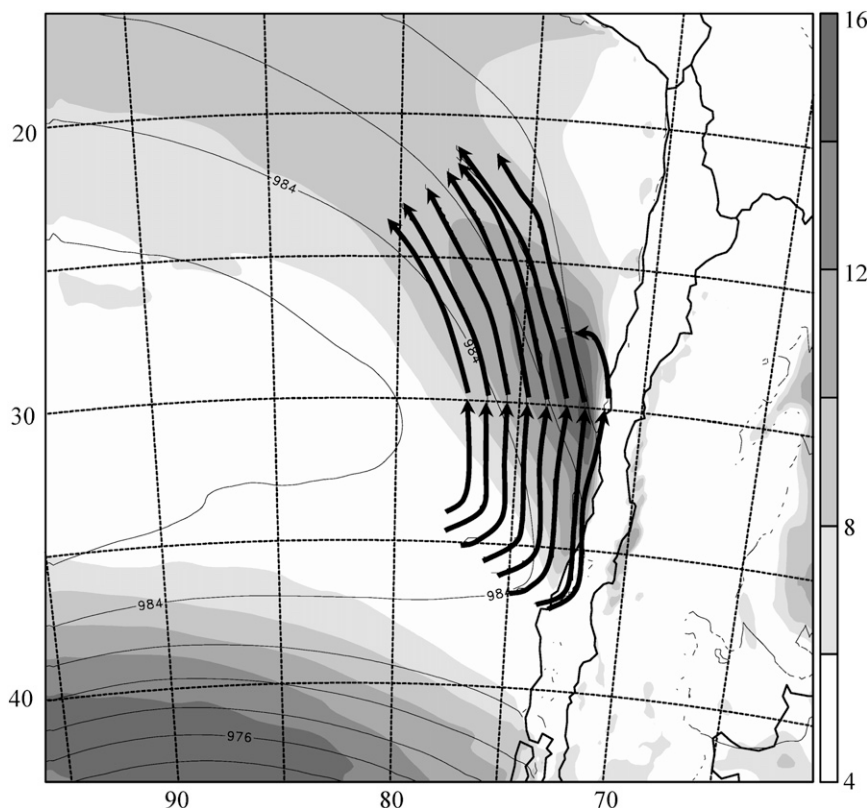
FIG. 11. As in Fig. 9, but for the weak-forcing case.

It is evident that the synoptic-scale forcing and the jet strength of the weak-forcing case are much weaker (Fig. 11) than the strong-forcing case (Fig. 9), and accordingly, the 30-h trajectories are shorter. In general, the parcels experience much less descent (Fig. 12), associated with weaker subsidence. It is evident that parcels closer to the coastline originate from higher altitudes and are noticeably warmer accordingly. Similar to the strong-forcing case, the geostrophic winds exhibit strong fluctuation. After removing the wave-related fluctuation, parcels seem to be in approximate geostrophic balance as they drift toward the jet maximum during the process of acceleration and descent. A more quantitative comparison between v and v_g is shown in Fig. 13. Regardless of the fairly large fluctuation of v_g, there is a clear trend that the parcels are supergeostrophic while descending through the MBL top inversion (i.e., the segment with v approximately in the range of 4–9 m s^{-1}), and become subgeostrophic after entering the viscous boundary layer (i.e., for $v > 9$ m s^{-1}).

b. Sensitivity simulations

The objective of these sensitivity simulations is to investigate the mesoscale response of the CLLCJ to changes in terrain height and surface heat flux. Ideally, we want the simulations to be long enough to allow for mesoscale adjustments and short enough to keep the synoptic-scale patterns similar for each set of sensitivity simulations. In the following analysis, only the last 24-h output from each simulation is used, and the first 24 h (i.e., the 12-h data assimilation cycle + the first 12 of the simulation) is considered the "spinup" period to allow initial perturbations induced by the terrain height or surface flux changes to disperse and propagate away.

Figure 14 shows that the synoptic-scale patterns over the SEP are almost identical for the four simulations of the strong-forcing event. For the strong-forcing jet, the reduction of the terrain to a quarter of the true terrain height results in a shorter and weaker CLLCJ (Figs. 14a,b). The jet core is located more offshore, in accordance with stronger easterlies in the inversion. The isobars are oriented more obliquely to the coastline over the jet area. The CLLCJ is further weakened in the NTRN run (Fig. 14c). The jet core moves farther offshore than the QTRN run, implying that the Andes inhibit the development of strong easterly winds and anchor the coastal baroclinic zone. It is noteworthy that the coastal MESOH disappears in the NTRN run, which confirms that the MESOH owes its existence to the interaction between the synoptic-scale flow and the
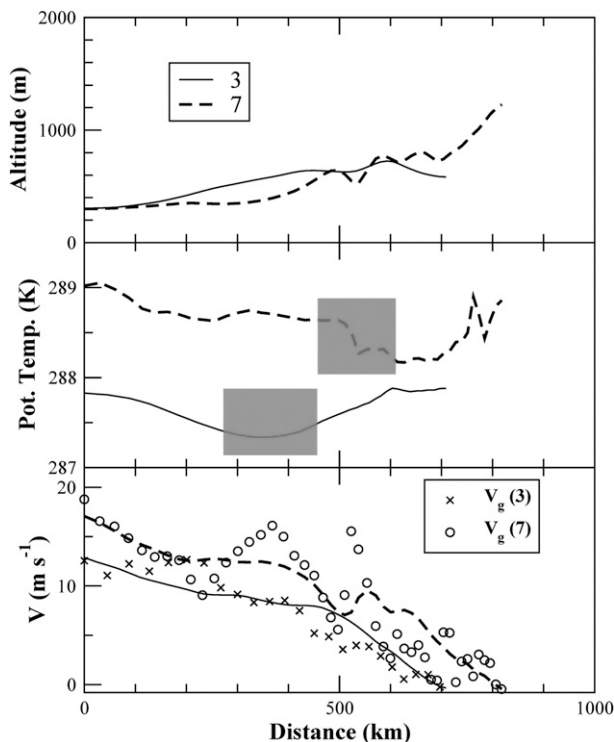
FIG. 12. As in Fig. 10, but for the weak-forcing case.

southern Andes. The jet strength at the surface is noticeably weaker in the SSHF run than in the CTRL run (Fig. 14d), but stronger than in the QTRN and NTRN simulations, suggesting that while the LSDH effect tends to enhance the CLLCJ, its impact on the CLLCJ is smaller than the terrain forcing effect. Also, the reduction in the land–sea sensible heat flux difference seems to have little impact on the strength and location of the coastal MESOH.

The jet strength aloft shows similar sensitivity to changes in the terrain height and sensible heat flux over land (Figs. 15 and 16). A few other features in the vertical cross sections in Figs. 15 and 16 are worth mentioning. Near the coastline, the heights of the BL top inversion and the jet core are progressively lower and the BL top inversion is progressively weaker with the decrease of the terrain height (Fig. 15). It is also noteworthy that above the BL, the elevated northerly winds are significantly weaker with the reduction or removal of the topography. In the SSHF run, both the CLLCJ and the elevated northerly jet above the BL are weaker than in the CTRL run, again, implying that the LSDH in general tends to enhance the coastal jets.

For the weak-forcing simulations, the change in terrain height or sensible heat flux over land has little impact on the synoptic-scale patterns far offshore over the integration time (Fig. 17). The coastal MESOH becomes
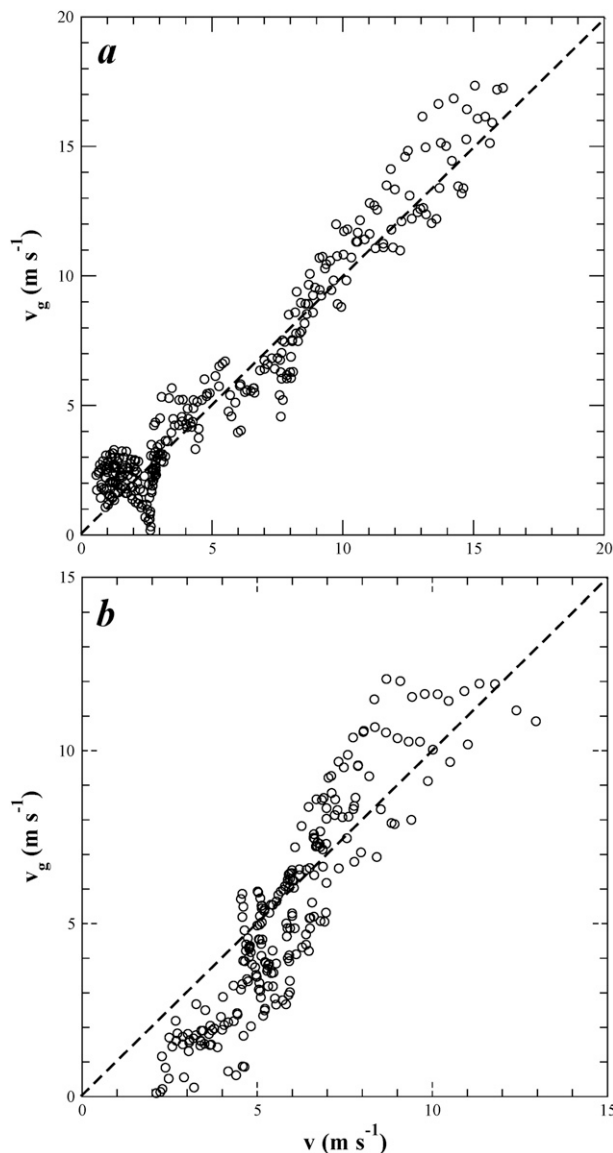

FIG. 13. Plot of the meridional geostrophic winds vs the meridional winds for set 1 parcels derived from (a) the strong-forcing case and (b) the weak-forcing case, respectively.

progressively weaker and shifts northward as the terrain height is reduced, implying weaker interaction between the SEPH and the Andes. The intensity of the CLLCJ decreases accordingly (Figs. 17 and 18). However, unlike the strong-forcing case, the orientation of the isobars over the jet is much less sensitive to the change of terrain height in the weak-forcing case. Compared to the strong-forcing jet, the easterlies in the MBL inversion are much less sensitive to the terrain height variation (Fig. 19), indicating that the Andes' role in inhibiting the coastal easterlies is insignificant for a weak-forcing jet. The jet intensity in the SSHF simulation is weaker than in the
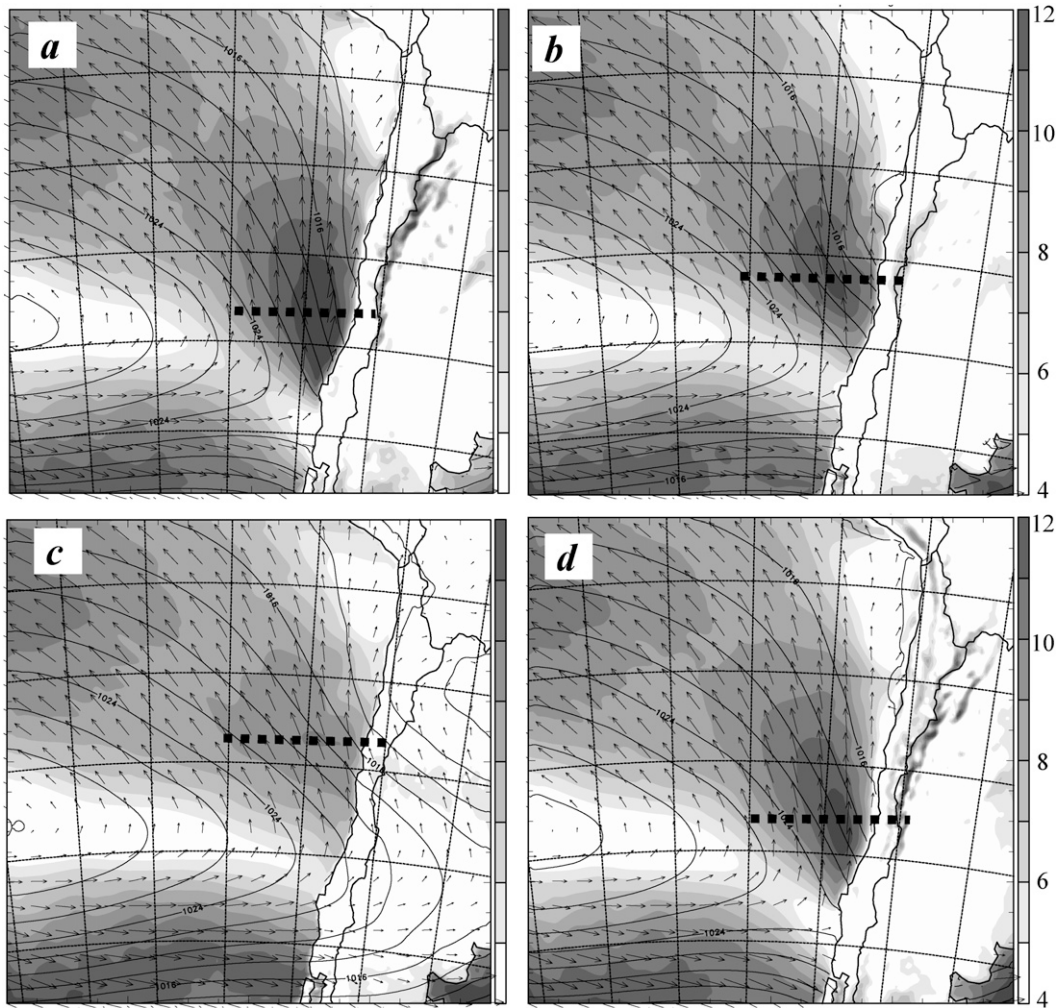
FIG. 14. The 10-m wind speed (grayscale, increment = 1 m s^{-1}), wind vectors, and surface pressure (contours, increment = 1 hPa), averaged over the 24-h period from 0000 UTC 22 Oct to 0000 UTC 23 Oct 2008 derived from (a) CTRL, (b) QTRN, (c) NTRN, and (d) SSHF simulations. The dashed lines indicate the locations of the vertical cross sections in Fig. 15.

CTRL run and comparable to that in the QTRN run (Figs. 17 and 18), implying that the LSDH effect plays a more important role in weak-forcing jets than in strong-forcing jets. It is worth noting that the 24-h profiles near the jet maximum (not shown) also show that the CLLCJ is noticeably supergeostrophic in the MBL top inversion and subgeostrophic in the viscous boundary layer for the two cases examined.

c. Linear decomposition

From the two sets of sensitivity simulations, we can crudely evaluate the relative importance of each process by assuming that the jet strength is a linear superposition of contributions from each process:

$$V_{\text{CTRL}} = F_{s+o} + F_T + F_{\text{SH}},$$

$$V_{\text{QTRN}} = F_{s+o} + \alpha F_T + F_{\text{SH}},$$

$$V_{\text{NTRN}} = F_{s+o} + F_{\text{SH}}, \quad \text{and}$$

$$V_{\text{SSHF}} = F_{s+o} + F_T, \tag{3}$$

where V_{CTRL}, V_{QTRN}, V_{NTRN}, and V_{SSHF} denote the CLLCJ strengths in terms of the maximum meridional wind components for the CTRL, QTRN, NTRN, and SSHF simulations. On the right-hand side, F_T, F_{SH}, and F_{S+O} represent the contributions from terrain forcing, LSDH effect, and synoptic-scale forcing (and other processes such as the difference in land–sea surface roughness), respectively. The quarter-terrain forcing on the CLLCJ is assumed to be a fraction of the whole terrain forcing, represented by the coefficient α.
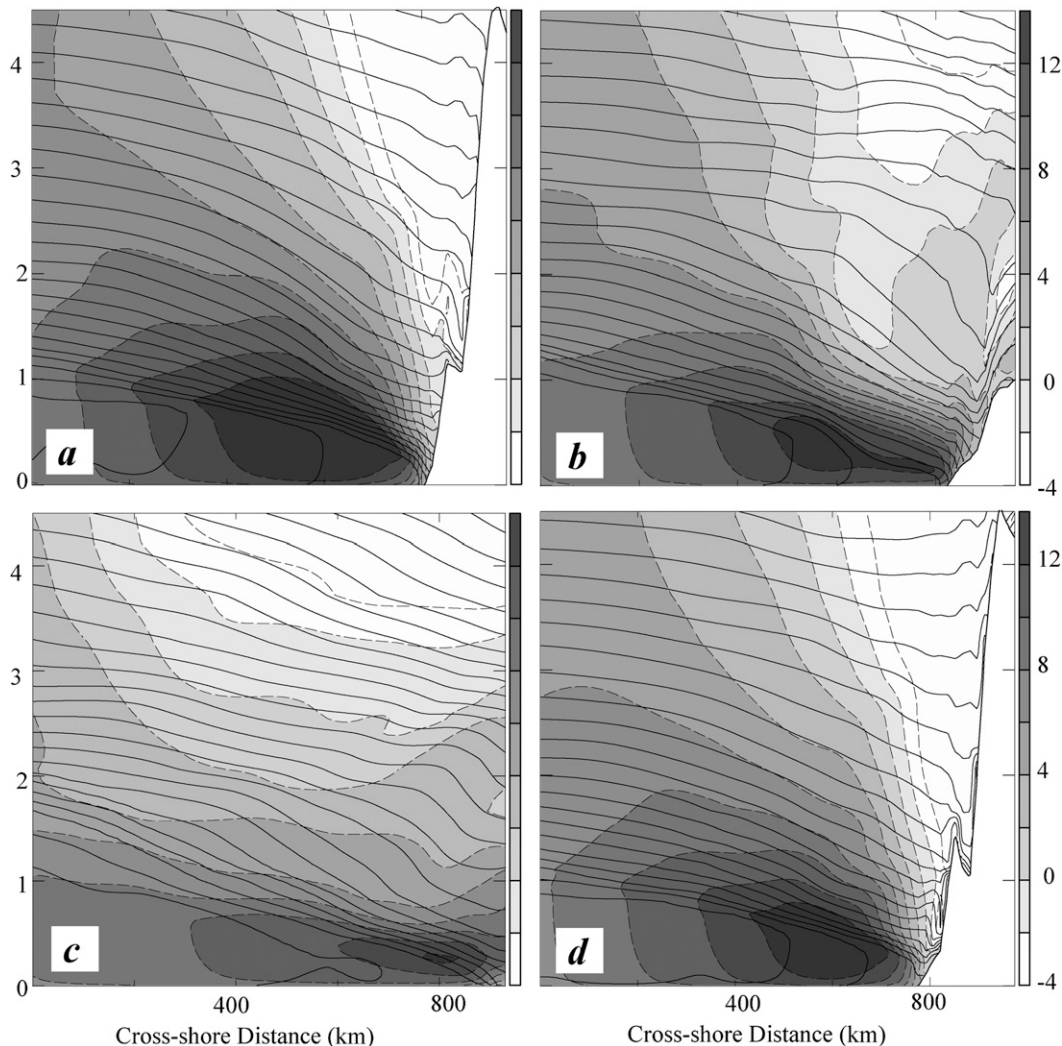
Fig. 15. Cross sections of the meridional wind component (grayscale and dashed contours, increment = 2 m s^{-1}) and potential temperature (solid contours, increment = 1 K) derived from the 24-h average of the (a) CTRL, (b) QTRN, (c) NTRN, and (d) SSHF simulations of the 22–23 October event. See Fig. 14 for the locations of the cross sections.

Nonlinear interactions between different processes have been ignored in (3). The solution to (3) normalized by the jet strength in the control simulation can be written as

$$F_T/V_{CTRL} = 1 - V_{NTRN}/V_{CTRL},$$

$$F_{SH}/V_{CTRL} = 1 - V_{SSHF}/V_{CTRL},$$

$$F_{S+o}/V_{CTRL} = (V_{NTRN} + V_{SSHF})/V_{CTRL} - 1, \quad \text{and}$$

$$\alpha = (V_{QTRN} - V_{NTRN})/(V_{CTRL} - V_{NTRN}).$$

$$(4)$$

The percentage contributions to the CLLCJ from the synoptic forcing, terrain, and LSDH effects for the two jet events, derived using the 24-h jet intensity from the two sets of simulations, are listed in Table 1. For both cases, the synoptic-scale forcing plays the primary role in driving the CLLCJ, accounting for more than 50% of the total contribution. The contribution from terrain forcing is second only to the synoptic-scale forcing. The LSDH effect plays a relatively minor role in the strong-forcing case. For the weak-forcing jet, the impact of the terrain becomes less significant and the contribution from the LSDH effect becomes nearly comparable to the terrain effect.

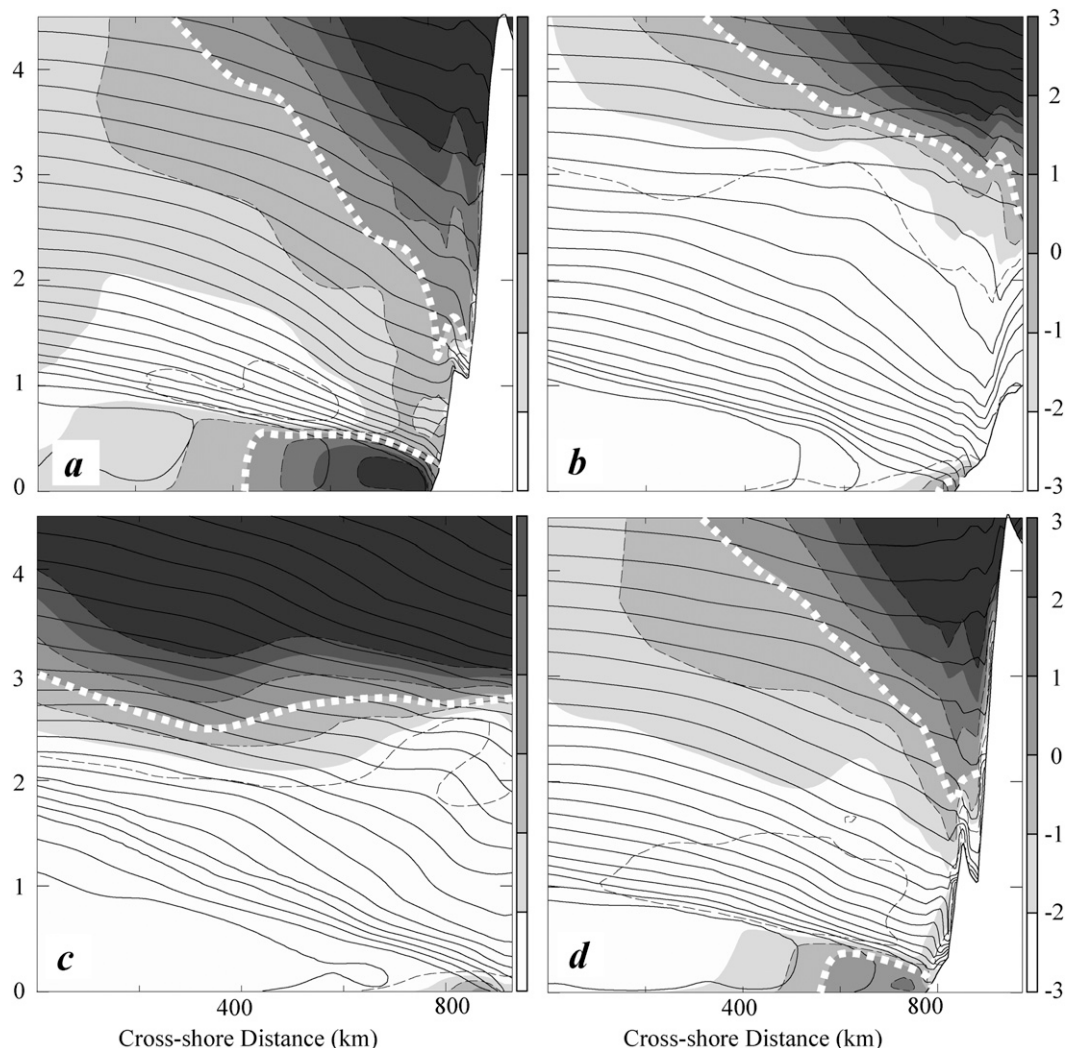In summary, the linear decomposition suggests that while the SEPH plays the primary role in driving the

FIG. 16. As in Fig. 5, but for the zonal wind component with an increment of 1 m s^{-1}. The white dashed contours correspond to $u = 0$.

CLLCJ, both the Andes and the LSDH have substantial contributions to the CLLCJ. The relative importance of the LSDH effect is dramatically different for the two types of jets. For a CLLCJ under strong synoptic-scale forcing, the dynamic interaction between the SEPH and the Andes dominates and the LSDH effect is small. For a weak-forcing jet, the LSDH is much more important. It is also noteworthy that the fractional terrain effect coefficient α is around ⅔ for both cases, implying that when the terrain height is reduced to one-quarter of the true terrain height, the terrain effect is only reduced to ⅔ of the full terrain effect. Finally, two caveats are worth mentioning here. First, the three forcing processes, synoptic-scale patterns, terrain, and LSDH, are virtually interweaved and it is impossible to completely separate them. For example, when reducing or removing the

topography, the large-scale forcing and the sensible heat flux over topography change accordingly. Therefore, an underlying assumption in the above discussion and linear decomposition is that the proportional changes in the synoptic-scale flows and surface heat flux due to the reduction or removal of the topography are small. Second, the above discussions are only valid for time scales of 1–2 days. Presumably, removing the Andes or reducing the sensible heat flux over land shall eventually lead to substantial changes in the large-scale flows over a longer time scale, which is beyond the scope of this study.

5. Discussion and conclusions

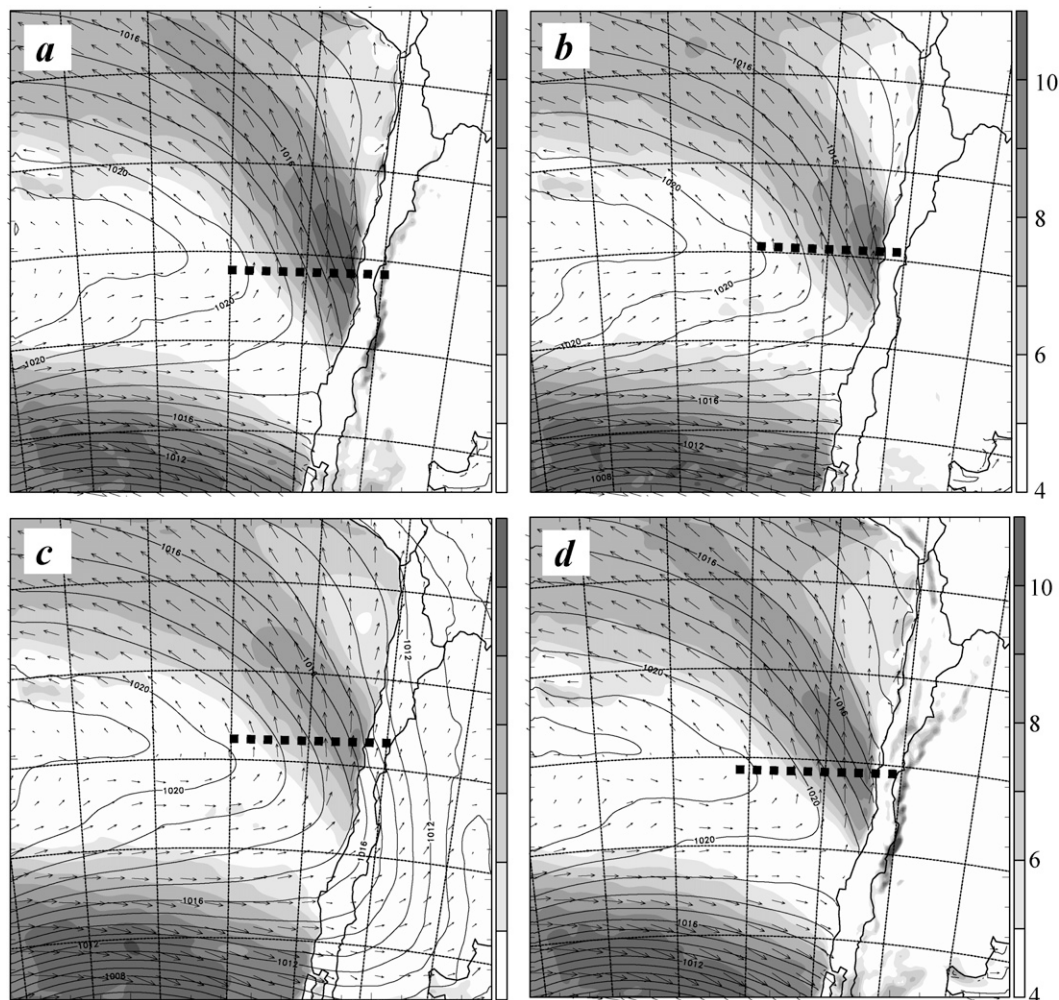Most of the COAMPS-simulated CLLCJ characteristics illustrated in this study, such as the CLLCJ intensity

FIG. 17. The 10-m wind speed (grayscale, increment = 1 m s^{-1}), wind vectors, and surface pressure (contours, increment = 1 hPa), averaged over a 24-h period from 0000 UTC 22 Nov to 0000 UTC 23 Nov 2008 derived from (a) CTRL, (b) QTRN, (c) NTRN, and (d) SSHF simulations. The dashed lines indicate the locations of the vertical cross sections in Fig. 18. See Fig. 17 for the locations of the cross sections.

and width, the jet core location, and the downward sloping of the MBL top inversion toward the coast, are consistent with previous studies of the CLLCJ or CCJ. The in-depth diagnosis of these simulations in sections 3–4 provides some additional perspectives on the mesoscale dynamics associated with the CLLCJ formation and adjustment processes, which are further discussed in this section. The discussion is centered around the following two issues: (i) the impact of the synoptic-scale forcing, topography, and LSDH on the CLLCJ; and (ii) the adjustment processes of the CLLCJ and the attendant cross-shore circulation.

Both the COAMPS real-time forecasts and the additional sensitivity simulations indicate that the synoptic-scale forcing, specifically, the SEPH, plays the primary role in driving the CLLCJ. Our study suggests that the

longitudinal location of the SEPH center is a useful index for the synoptic-scale forcing. When the SEPH is located closer to the Chilean coast, the CLLCJ, as one of the circulation branches around the SEPH center, is stronger. In addition, the interaction between the SEPH circulation and the Andes results in a more pronounced mesoscale high pressure offshore of the southern Chilean coast (i.e., ~40°S). The mesoscale high, largely due to the terrain blocking of the midlatitude westerlies, increases the equatorward pressure gradient force and further enhances the CLLCJ. The Andes intensify the CLLCJ mainly through three dynamical processes: creating the coastal MESOH by blocking the midlatitude westerlies, inhibiting the full development of the cross-shore flow (i.e., easterlies) and therefore anchoring the baroclinic zone along the central Chilean coast, and
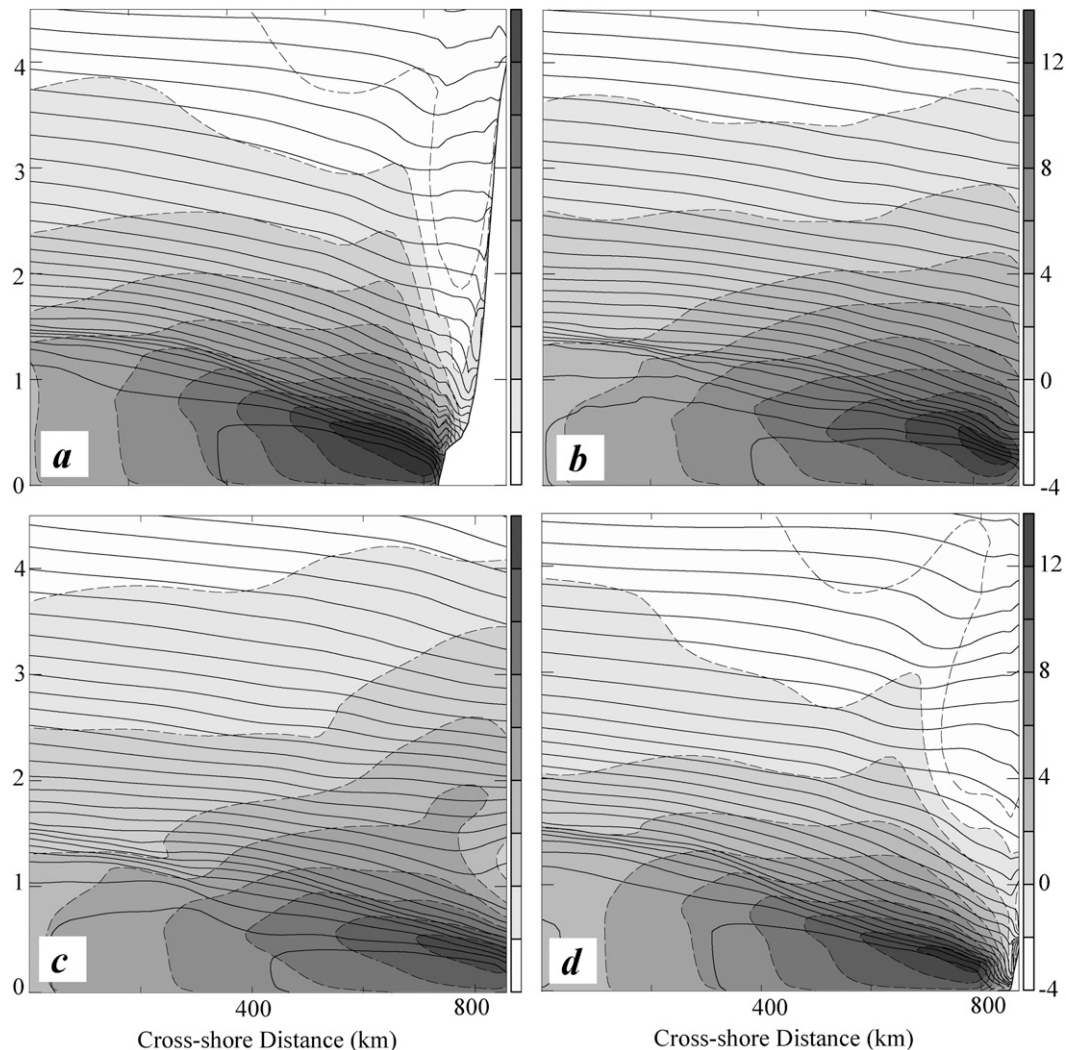
FIG. 18. Cross sections of the meridional wind component (grayscale and dashed contours, increment = 2 m s^{-1}) and potential temperature (solid contours, increment = 1 K) derived from the 24-h average of the (a) CTRL, (b) QTRN, (c) NTRN, and (d) SSHF simulations of the 22–23 Nov 2008 event.

contributing to the coastal low formation to the northwest of the CLLCJ. The land–sea differential heating (LSDH) tends to enhance the CLLCJ mainly through strengthening coastal baroclinicity and its impact on the CLLCJ is in general smaller than the Andes. The relative importance of the LSDH and the topography varies with the synoptic conditions. Compared with strong-forcing jets, the interaction between the SEPH and the Andes for weak-forcing jets is much weaker and the resultant MESOH is less pronounced. The relative importance of the LSDH increases accordingly.

The intensity of the CLLCJ is positively correlated with the pressure difference between the MEOSH to its south and the coastal low (CL) to the north, suggesting that the south–north pressure gradient force intensifies

the CLLCJ. Inspection of the cross-jet momentum balance in the CLLCJ indicates that flow within the MBL top inversion is slightly supergeostrophic and, beneath the inversion, the viscous BL flow is subgeostrophic. In summary, the COAMPS simulations suggest the following geostrophic adjustment process for the CLLCJ. In the vicinity of the MESOH, as parcels descend into the lower troposphere (~2–3 km), they are accelerated by the northward pressure gradient force associated with the MESOH and CL. The small resultant force in the nearly inviscid inversion layer induces a weak easterly flow along the coast. The easterly flow creates a divergence zone, which enhances subsidence along the coast, as required by conservation of mass. Consequently, the adiabatic warming associated with the enhanced
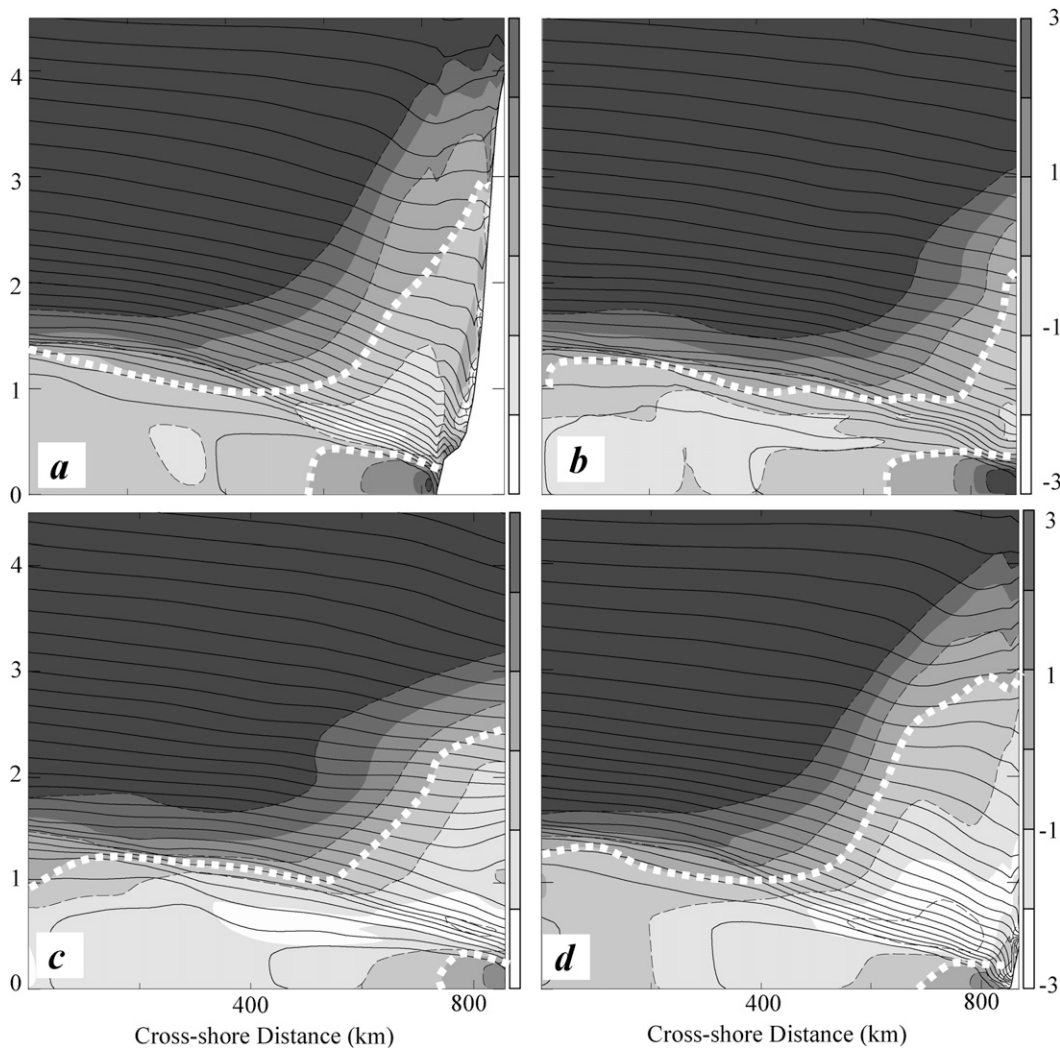
FIG. 19. As in Fig. 18, but for the zonal wind component with an increment of 1 m s^{-1}.

subsidence along the coast reduces the low-level pressure and further increases the cross-shore pressure gradient, which tends to balance the Coriolis force. The strength of a coastal low resulted from geostrophic adjustment of a coastal jet can be estimated as $P' = -\rho_{air}fvL_y$. Using the air density $\rho_{air} \sim 1$ kg m^{-3}, the jet width $L_y \sim 300$ km, mean jet strength $v \sim 10$ m s^{-1}, and $f \sim 10^{-4}$ s^{-1}, we obtain a scale estimate of the coastal low pressure $P' \sim 3$ hPa, which is comparable to previous studies (Garreaud et al. 2002). However, a question arises from the scale analysis. The typical horizontal scale of the CLLCJ is of the order of 1000 km, which is several times larger than the Rossby radius of deformation given by $L_R = V/f \sim 10$ m s^{-1}/10^{-4} s$^{-1} \sim 100$ km. From the geostrophic adjustment perspective, one should expect the CLLCJ to be in close geostrophic balance and the velocity adjustment dominates the mass (i.e., pressure) adjustment.

The apparent inconsistency between the model results and the scale analysis is due to the strong subsidence over the CLLCJ, which introduces a new horizontal scale. As demonstrated in the trajectory analysis in section 4a, a parcel is only subjected to geostrophic adjustment during its descent through the MBL top inversion, which occurs typically over a horizontal distance on the order of 100 km (Figs. 10 and 12) and is comparable to the Rossby radius of deformation. Therefore, both mass and velocity adjustments are equally important in the CLLCJ geostrophic adjustment process. It also implies that classic two-dimensional geostrophic adjustment theory may not be applicable to subtropical coastal jet adjustment processes characterized by significant descent.

A closely related issue is the applicability of reduced shallow-water theory (RSWT) to subtropical coastal jets. RSWT has been widely used in studies of interactions

TABLE 1. Linear decomposition of contributions to the CLLCJ from synoptic forcing, terrain, and LSDH effects derived from the two sets of sensitivity simulations.

Processes	Strong forcing	Weak forcing
Synoptic and others	58%	55%
Terrain	35%	26%
Differential heating	7%	19%
α	2/3	2/3

between the marine BL flow and coastal topography (e.g., Gill 1977; Chao 1985; Samelson 1992). The applicability of the RSWT to subtropical coastal jets can be justified by the frequent presence of the well-defined marine BL top inversion, which decouples the MBL flow from the free atmosphere. However, the conservations of mass and momentum in RSWT require that the cross-inversion mass entrainment rate is small compared to the bulk mass flux in the marine BL [i.e., $w_e/(UH)_x \ll 1$ or $L \ll UH/w_e$, where L is the characteristic horizontal scale of the dynamical process under study]. Assuming $U = 10$ m s^{-1}, $H = 500$ m, $w_e = 5$ mm s^{-1}, and $L_{max} = 0.1UH/w_e$, we obtain the maximum length scale for RSWT to be valid is of the order of 100 km. According to this scaling, RSWT is a reasonable approximation for the study of hydraulic jumps and expansion fans along the California coast, the typical scales of which are 100 km or less. However, one should be cautious to apply RSWT to the CLLCJ and CCJ adjustment processes, the characteristic horizontal scales of which are typically of the order of 500–1000 km. It is also worth noting that much stronger coastal jets have been documented offshore of the California coast ($\sim$30 m s^{-1}; Zemba and Friehe 1987), due to the acceleration associated with hydraulic responses of the marine boundary layer to the promontories along the California coast.

REFERENCES

Bakun, A., 1990: Coastal ocean upwelling. *Science,* **247,** 198–201.

——, and C. S. Nelson, 1991: The seasonal cycle of wind-stress curl in subtropical eastern boundary current regions. *J. Phys. Oceanogr.,* **21,** 1815–1834.

Bielli, S., P. Barbour, R. Samelson, R. Skyllingstad, and J. Wilczak, 2002: Numerical study of the diurnal cycle along the central Oregon coast during summertime northerly flow. *Mon. Wea. Rev.,* **130,** 992–1008.

Burk, S. D., and W. T. Thompson, 1996: The summertime low-level jet and marine boundary layer structure along the California coast. *Mon. Wea. Rev.,* **124,** 668–686.

Chao, S., 1985: Coastal jets in the lower atmosphere. *J. Phys. Oceanogr.,* **15,** 361–371.

Cui, Z., M. Tjernstrom, and B. Grisogono, 1998: Idealized simulations of atmospheric coastal flow along the central coast of California. *J. Appl. Meteor.,* **37,** 1332–1363.

Ebuchi, N., H. C. Graber, and M. J. Caruso, 2002: Evaluation of wind vectors observed by QuikSCAT/SeaWinds using ocean buoy data. *J. Atmos. Oceanic Technol.,* **19,** 2049–2062.

Fairall, C., F. Bradley, D. P. Rogers, J. B. Edson, and G. S. Young, 1996: Bulk parameterization of air–sea fluxes for Tropical Ocean Global Atmosphere Coupled Ocean–Atmosphere Response Experiment. *J. Geophys. Res.,* **101,** 3747–3764.

Fu, Q., K. N. Liou, M. C. Cribb, T. P. Charlock, and A. Grossman, 1997: Multiple scattering parameterization in thermal infrared radiative transfer. *J. Atmos. Sci.,* **54,** 2799–2812.

Garreaud, R. D., and J. A. Rutllant, 2003: Coastal lows along the subtropical West Coast of South America: Numerical simulation of a typical case. *Mon. Wea. Rev.,* **131,** 891–908.

——, and R. C. Muñoz, 2005: The low-level jet off the west coast of subtropical South America: Structure and variability. *Mon. Wea. Rev.,* **133,** 2246–2261.

——, J. A. Rutllant, and H. Fuenzalida, 2002: Coastal lows along the subtropical coast of South America: Mean structure and evolution. *Mon. Wea. Rev.,* **130,** 75–88.

Gill, A. E., 1977: Coastally trapped waves in the atmosphere. *Quart. J. Roy. Meteor. Soc.,* **103,** 431–440.

Haack, T., and S. D. B. Burk, 2001: Summertime marine refractivity conditions along coastal California. *J. Appl. Meteor.,* **40,** 673–687.

Hodur, R. M., 1997: The Naval Research Laboratory's Coupled Ocean/Atmospheric Mesoscale Prediction System (COAMPS). *Mon. Wea. Rev.,* **125,** 1414–1430.

Josey, S. A., E. C. Kent, and P. K. Taylor, 2002: Wind stress forcing of the ocean in the SOC climatology: Comparisons with the NCEP–NCAR, ECMWF, UWM/COADS, and Hellerman and Rosenstein datasets. *J. Phys. Oceanogr.,* **32,** 1993–2019.

Kain, J. S., and J. M. Fritsch, 1993: Convective parameterization for mesoscale models: The Kain–Fritsch scheme. *The Representation of Cumulus Convection in Numerical Models, Meteor. Monogr.,* No. 46, Amer. Meteor. Soc., 165–170.

Liu, M., J. E. Nachamkin, and D. L. Westphal, 2009: On the improvement of COAMPS weather forecasts using an advanced radiative transfer model. *Wea. Forecasting,* **24,** 286–306.

Liu, W. T., and W. Tang, 1996: Equivalent neutral wind. JPL Publ. 96-17, Jet Propulsion Laboratory, Pasadena, CA, 8 pp.

Mears, C. A., D. K. Smith, and F. J. Wentz, 2001: Comparison of Special Sensor Microwave Imager and buoy-measured wind speeds from 1987 to 1997. *J. Geophys. Res.,* **106** (C6), 11 719–11 729.

Mellor, G. L., and T. Yamada, 1974: A hierarchy of turbulence closure models for planetary boundary layers. *J. Atmos. Sci.,* **31,** 1791–1806.

Muñoz, R. C., 2008: Diurnal cycle of surface winds over the subtropical southeast Pacific. *J. Geophys. Res.,* **113,** D13107, doi:10.1029/2008JD009957.

——, and R. D. Garreaud, 2005: Dynamics of the low-level jet off the west coast of subtropical South America. *Mon. Wea. Rev.,* **133,** 3661–3677.

Pomeroy, K. R., and T. R. Parish, 2001: A case study of the interaction of the summertime coastal jet with the California topography. *Mon. Wea. Rev.,* **129,** 530–539.

Portabella, M., and A. Stoffelen, 2009: On Scatterometer ocean stress. *J. Atmos. Oceanic Technol.,* **26,** 368–382.

Rogerson, A. M., 1999: Transcritical flows in the coastal marine atmospheric boundary layer. *J. Atmos. Sci.,* **56,** 2761–2779.

Rutledge, S. A., and P. V. Hobbs, 1983: The mesoscale and microscale structure of organization of clouds and precipitation in midlatitude cyclones. VIII: A model for the ''seeder-feeder'' process in warm-frontal rainbands *J. Atmos. Sci.,* **40,** 1185–1206.

Samelson, R. M., 1992: Supercritical marine-layer flow along a smoothly varying coastline. *J. Atmos. Sci.,* **49,** 1571–1584.

Stensrud, D. J., 1996: Importance of low-level jets to climate: A review. *J. Climate,* **9,** 1698–1711.

Thompson, W. T., and S. D. Burk, 1991: An investigation of an Arctic front with a vertically nested mesoscale model. *Mon. Wea. Rev.,* **119,** 233–261.

Wang, S., Q. Wang, and J. Doyle, 2002: Some improvement of Louis surface flux parameterization. Preprints, *15th Symp. on Boundary Layers and Turbulence,* Wageningen, Netherlands, Amer. Meteor. Soc., 547–550.

Woods, R., and Coauthors, 2007: VOCALS: The VAMOS Ocean–Cloud–Atmosphere–Land Study: Improving understanding, model simulations, and prediction of the Southeast Pacific Climate System. NCAR Earth Observing Laboratory, 9 pp. [Available online at http://www.eol.ucar.edu/projects/vocals/documentation/vocals_overview.pdf.]

Zemba, H., and C. A. Friehe, 1987: The marine atmospheric boundary layer jet in the Coastal Ocean Dynamics Experiment. *J. Geophys. Res.,* **92,** 1489–1496.